TÜRKİYE CUMHURİYETİ
ADANA ALPARSLAN TÜRKEŞ SCIENCE AND TECHNOLOGY UNIVERSITY

GRADUATE SCHOOL
ELECTRICAL AND ELECTRONIC ENGINEERING DEPARTMENT

ALL GAN-BASED MULTIDEVICE INTERLEAVED BOOST CONVERTER STRUCTURE FOR HYBRID ELECTRIC VEHICLES

ALİ ZÜLFİKAROĞLU

M.Sc.

ADANA 2023

TÜRKİYE CUMHURİYETİ
ADANA ALPARSLAN TÜRKEŞ SCIENCE AND TECHNOLOGY UNIVERSITY

GRADUATE SCHOOL
ELECTRICAL AND ELECTRONIC ENGINEERING DEPARTMENT

ALL GAN-BASED MULTIDEVICE INTERLEAVED BOOST CONVERTER STRUCTURE FOR HYBRID ELECTRIC VEHICLES

ALİ ZÜLFİKAROĞLU

M.Sc.

THESIS ADVISOR
Asst. Prof. Dr. Amira TANDİROVİÇ GÜRSEL

ADANA, 2023

ÖZET

ELEKTRİKLİ ARAÇLAR İÇİN TÜMÜ GAN TABANLI ÇOK CİHAZLI SERPİŞTİRİLMİŞ YÜKSELTİCİ DÖNÜŞTÜCÜ YAPISI

Ali ZÜLFİKAROĞLU
Yüksek Lisans, Elektrik-Elektronik Mühendisliği Anabilim Dalı
Danışman: Dr. Öğr. Üyesi Amira TANDİROVİÇ GÜRSEL
Haziran 2023, 67 sayfa

Sera gazı emisyonlarının azaltılması, küresel ulaşımda fosil yakıtların kullanımını azaltmak için sürekli bir yaklaşım gerektirir. Çevre dostu olmaları, verimlilikleri, sessizlikleri ve uzun vadeli sürdürülebilirlik potansiyelleri nedeniyle elektrikli araçlar, içten yanmalı motorlarla çalışan araçlara uygun bir alternatiftir. Elektrikli araçların artan popüleritesine rağmen, geleneksel araçlarla başarılı bir şekilde rekabet edebilmek için maliyet, kapasite, sürüş menzili, enerji kayıpları ve güç aktarma teknolojileri gibi alanlarda hala önemli ilerlemelere ihtiyaçları var. Bu nedenle, mimari ve verimlilik açısından güç iletimindeki ilerlemeler, on yıllardır bilim camiasının ön planında yer almaktadır. Doğru akımdan doğru akıma (DC'den DC'ye) dönüştürücüler, güç tüketimini azaltmak için optimize edilebilen, böylece enerji verimliliğini artıran, boyutları azaltılabilen ve böylece kompaktlık sağlayan devre bileşenlerine bir örnektir.

Uygun bileşen seçimi ile birlikte devre sisteminin minyatürleştirilmesi ve hafif yapısal malzemelerin kullanımı, daha ucuz, daha duyarlı ve gelişmiş güvenilirliğe sahip sistemlerle sonuçlanabilir. İndüktör ve kapasitör gibi pasif bileşenler, sırasıyla giriş akımı ve çıkış voltajı dalgalanmalarını düzeltmeyi amaçlayarak dönüştürücü topolojilerinde çok önemli bir rol oynamaktadır. Ancak o kadar büyüktürler ki dönüştürücü için ayrılan alanın çoğunu kaplamaktadırlar. Bu nedenle, kullanılan pasif bileşenlerin sayısını ve minyatürleştirilmesini azaltmaya yönelik her türlü çaba, dönüştürücü teknolojisi için önemli bir ilerlemeyi temsil etmektedir. Galyum nitrür (GaN) ve silisyum karbür (SiC), son teknoloji verimli güç dönüştürücü cihazları tasarlamak için uygun olan geniş bant aralıklı yarı iletken malzemelerin iki örneğidir. Bu yarı iletkenlerin geniş bant aralığı, yüksek kritik parçalanma elektrik alanı, daha yüksek elektron hızı ve yüksek termal iletkenlik gibi özellikleri, pasif bileşenlerin boyutunda önemli ölçüde azalmaya, soğutucunun küçülmesine ve dönüştürücünün güç yoğunluğunun artmasına olanak tanır.

Bu tezde, 2010 Toyota Prius Si-IGBT tabanlı yükseltici dönüştürücü topolojisi araştırılmış ve PSpice simülasyon yazılımı yardımıyla simüle edilmiştir. Bundan sonra, bu dönüştürücü yapısı, sırasıyla SiC ve GaN yarı iletkenlerini uygulanmasıyla çok cihazlı serpiştirmeli yükseltici dönüştürücü (MDIBC) topolojisi ile yeniden yapılandırıldı. SiC tabanlı ve GaN tabanlı MDIBC topolojilerinin performansını güç kaybı, verimlilik, pasif bileşenlerin boyutu ve ayrıca akım ve voltaj dalgalanmaları açısından analiz etmek için değişen anahtarlama frekanslarında iki önemli vaka çalışması kullanıldı. Her iki durumda da önemli ölçüde azaltılmış akım ve gerilim dalgalanmalarına rağmen pasif bileşenlerin daha düşük değerlerine ulaşılmıştır. GaN tabanlı MDIBC ile tüm anahtarlama frekanslarında elde edilen daha yüksek verimlilik sonuçlarının aksine, SiC tabanlı MDIBC, referans dönüştürücüye kıyasla 80 ve 100 kHz'de daha düşük değerlerle sonuçlandı. Önerilen GaN tabanlı MDIBC, ilk durumda akım için dalgalanmayı %93,4 ve voltaj için %40, ikinci durumda 100 kHz anahtarlama frekansında indüktör değeri için %88,5 ve kondansatör değeri için %97,92 azaltarak kıyaslama dönüştürücüsünden daha yüksek verim elde edildi.

Anahtar Kelimeler: akım ve voltaj dalgalanmaları, çok cihazlı serpiştirmeli yükseltici dönüştürücü (MDIBC), hibrit elektrikli araçlar, SiC ve GaN yarı iletkenler, verimlilik

ABSTRACT

ALL GAN-BASED MULTIDEVICE INTERLEAVED BOOST CONVERTER STRUCTURE FOR HYBRID ELECTRIC VEHICLES

Ali ZÜLFİKAROĞLU
M.Sc., Department of Electrical and Electronic Engineering
Supervisor: Asst. Prof. Dr. Amira TANDİROVİÇ GÜRSEL
June 2023, 67 pages

Greenhouse gas emissions reduction requires an ongoing approach to decreasing the use of fossil fuels in global transportation. Due to their environmental friendliness, efficiency, quietness, and potential for long-term sustainability, electric vehicles (EVs) are a viable alternative to those powered by internal combustion engines (ICE). Despite the rising popularity of EVs, they still need significant advancements in areas such as cost, capacity, driving range, energy losses, and powertrain technologies in order to successfully compete with conventional vehicles. Therefore, advancements in power transmission in terms of architecture and effectiveness have been in the foreground of the scientific community for decades. Direct current to direct current (DC/DC) converters are one example of circuit components that can be optimized to reduce power consumption, thereby enhancing energy efficiency, decreasing size, and thus providing compactness.

Miniaturization of circuitry, together with proper component selection and the use of lightweight structural materials, might result in cheaper, more responsive systems with improved reliability. Passive components such as inductors and capacitors play a crucial role in converter topologies that aim to smooth out input current and output voltage ripples, respectively. However, they are so large that they occupy the majority of the space reserved for the converter. Therefore, any effort to reduce the number of passive components used and their miniaturization represents a significant advancement for converter technology. Gallium nitride (GaN) and silicon carbide (SiC) are two examples of wide band gap semiconductor materials that are suited for designing state-of-the-art efficient power converter devices. These semiconductors' features, such as their large bandgap, high critical breakdown electric field, high thermal conductivity and higher electron velocity allow a considerable reduction in the size of passive components, shrinking the heatsink and an increase in the converter's power density.

In this thesis, the 2010 Toyota Prius Si-IGBT-based boost converter topology was investigated and simulated with the help of PSpice simulation software. After that, this converter structure was reconstructed with a multidevice interleaved boost converter (MDIBC) topology with implementing SiC and GaN semiconductors, respectively. Two prominent case studies with varying switching frequencies were utilized to analyze the performance of the SiC-based and GaN-based MDIBC topologies in terms of power loss, efficiency, the size of the passive components, as well as the current and voltage ripples. In both cases, it was achieved lower values of the passive components despite the relatively reduced current and voltage ripples. In contrast to the higher efficiency results achieved with GaN-based MDIBC at all switching frequencies, SiC-based MDIBC resulted in lower values at 80 and 100 kHz compared to the benchmark converter. Proposed GaN-based MDIBC achieved higher efficiency than the benchmark converter by lowering ripple by 93.4% for current and 40% for voltage in the first case, and by 88.5% for inductor value and 97.92% for capacitor value at 100 kHz switching frequency in the second case.

Keywords: current and voltage ripples, efficiency, hybrid electric vehicles, multidevice interleaved boost converter, SiC and GaN semiconductors

To my family

ACKNOWLEDGEMENTS

I would like to start with expressing my deepest gratitude to my supervisor Asst. Prof. Amira Tandiroviç Gürsel. My supervisor was more than simply a teacher; she demonstrated the perseverance, diligence, and maternal qualities a mother would have in raising her child in the best possible manner. She pushed me along this road and gave me the impression that I could always do better. Words alone cannot express my thanks to her for this as well.

I am also thankful to my friend Orçun Şen whom I studied together at the Denmark Technical University for inspiring me choosing this thesis topic. I learned many things from him about this research and motivated me whenever I need in this long process.

I am also grateful to one of my best friends Mehmet Kızılaslan for believing in me always and struggling for my success. Thanks should also go to my colleagues Şenol Şahin, Osman Güven, İlker Tanış, Hilmi Tagar, Arman Mavruk and Ayşim Zümrüt Yüksel for their close friendship, motivation and interest during this process.

Finally, this endeavor would not have been possible without my mother Sevgi Zülfikaroğlu, my father Adnan Zülfikaroğlu and my sister İrem Zülfikaroğlu. When I felt like giving up, they would encourage me and help me regain faith on a brighter day. They were as tired as they wrote a thesis in this process, but they gave their support every single day.

TABLE OF CONTENTS

LIST OF FIGURES

LIST OF TABLES

1. INTRODUCTION

1.1. Greenhouse Gases, Effects, And Mitigating Strategies

Greenhouse gases (GHGs) are gases that are able to absorb infrared light and retain it in the atmosphere as heat. The Kyoto protocol identifies Methane (CH4), Nitrous Oxide (N2O), Carbon dioxide (CO2), Hydrofluoride carbons (HFCs), Sulfurhexade fluoride (SF6), and Perfluorocarbons (PFCs) as the most significant GHGs. The process of heat-trapping by GHG, commonly known as the greenhouse effect, is a natural mechanism that warms the planet by capturing a portion of the sun's energy and maintaining a suitable temperature for life. Yet, the excessive emission of GHG results in significant increases in the amount of heat trapped in the atmosphere, and this additional heat is the cause of climate change.

Climate change may cause serious crises around the world. With the increase in high temperatures and drought, large-scale forest fires seen in the world have been increasing rapidly. The most obvious example of this was experienced in Australia in 2019. As a result of extremely hot and dry weather, the fire that started in June lasted 240 days, and thousands of hectares of forests were destroyed. As the temperature increases, the evaporation in the seas, lakes, and streams increases, and the evaporating water causes more rain, floods, landslides, and hurricanes. In addition, glaciers are melting rapidly, and melting glaciers cause sea levels to rise and land losses. Along with the melting glaciers, the living ecosystem in the poles is also damaged. Land losses caused by drought or floods may lead to devastating consequences such as food shortages, starvation, and malaria. These reasons caused by climate change make the world even more unlivable. Therefore, according to scientists, Earth’s temperature increase should be brought under control as soon as possible and limited to 2°C.

In order to control the effects of climate change and limit temperature rise, the transportation sector stands out as one of the most important factors to be considered. Because the usage of petroleum products and fossil fuels like gasoline, diesel, and natural gas has increased steadily over the last century, there has been a significant rise in the emission of GHGs, which are thought to be the cause of global warming [1, 2]. Although they are not the sole, conventional vehicles, especially those used in road transport which accounts for 16% of global emissions, are seen as the main culprits for this increase.

According to the Antalya Chamber of Commerce news dated October 2021, 29% of total emissions in the United States and 25% of total emissions in the European Union came from the transportation sector in 2019. Considering the negative effects of these emissions on global warming, with the 2015 Paris Climate Agreement, countries set concrete targets to reach net-zero emissions, keep the impact of global warming below 2 °C, and limit it to 1.5 °C if possible. For this purpose, the European Union has set a target to reach net-zero emissions by 2050. On the other hand, Turkey officially ratified the Paris Agreement on October 7, 2021, committing to reach net-zero emissions by 2053. In order to reach net-zero emissions and keep global warming at the determined values, serious steps must be taken in various areas, and strategies must be determined in this direction [3].

Developing a sustainable approach for lowering the usage of fossil fuels in global transportation is crucial for reducing GHG emissions. Nonetheless, it is regarded as one of the most difficult undertakings on a global basis. Assuming that fossil fuels are still a cheap and dependable source to create energy, it is not likely to stop developing those tendencies without enacting significant and ongoing mitigation actions. In this perspective, the Doha Amendment to the Kyoto Protocol, which was signed in 2012, is one of the most important steps ahead, since it has become vital to replace traditional cars with more environmentally friendly technology, such as EVs.

1.2. Overview Of Electric Vehicles And Their Benefits On The Environment

EVs are vehicles getting their power, in whole or in part, from rechargeable batteries. It should be noted that battery power is not a new innovation, and it has been a part of the automobile mentality for as long as gas-powered technology has been. The quick increase in popularity is largely attributable to the perception that they are suitable candidates for decreasing carbon emissions [4].

Vehicle tailpipe emissions are the GHG emission produced by chemicals that arise as a result of the combustion of fuel used in vehicles. While All-electric vehicles, also known as Battery Electric Vehicles (BEVs), have zero tailpipe emissions, Hybrid Electric Vehicles (HEVs) and Plug-in Hybrid Electric Vehicles (PHEVs) generate tailpipe emissions while using fuel. Since BEVs have no tailpipe emissions, they produce no carbon dioxide emissions while driving. This reduces air pollution considerably. However, the electricity that is produced to charge EVs may create GHG emissions. The generation of electricity to charge EVs is a significant source of GHG emissions. The amount of these emissions varies depending on the source of the electrical energy produced. For example, while these emissions are higher in the electrical energy produced using coal and natural gas, with producing by solar and wind, they are low. Therefore, increasing renewable energy-based electricity generation may result in lower GHG emissions associated with EVs [5].

The manufacturing process of EVs can generate more emissions than the manufacturing of conventional vehicles. This is due to the energy used in obtaining lithium in the battery production phase. Figure 1.1 shows the estimated emissions of researchers at Argonne National Laboratory for a gasoline car and an EV with an electric range of 300 miles. The assumptions represent the model year 2020. The blue bar represents emissions linked with the battery. GHG emissions generated in the battery production process in EVs constitute 18% of the total emissions. The orange bar represents the emissions generated by the manufacturing process of vehicles. For EVs, this proportion is about 17%, while for gasoline cars, this ratio is about only 9%. Emissions from the production of gasoline or electricity (U.S. mix) are shown in the gray bars. Considering the gray bar proportions, the proportions are significantly higher for EVs. While 65% of the electricity production provided by EVs, 17% of fuel production and distribution comes from gasoline cars. The yellow line depicts emissions from the vehicle's tailpipe in a ratio of 74%. Looking at these ratios, we can clearly say that the life cycle GHG emissions associated with EVs are typically lower than that of average gasoline-powered vehicles [6].

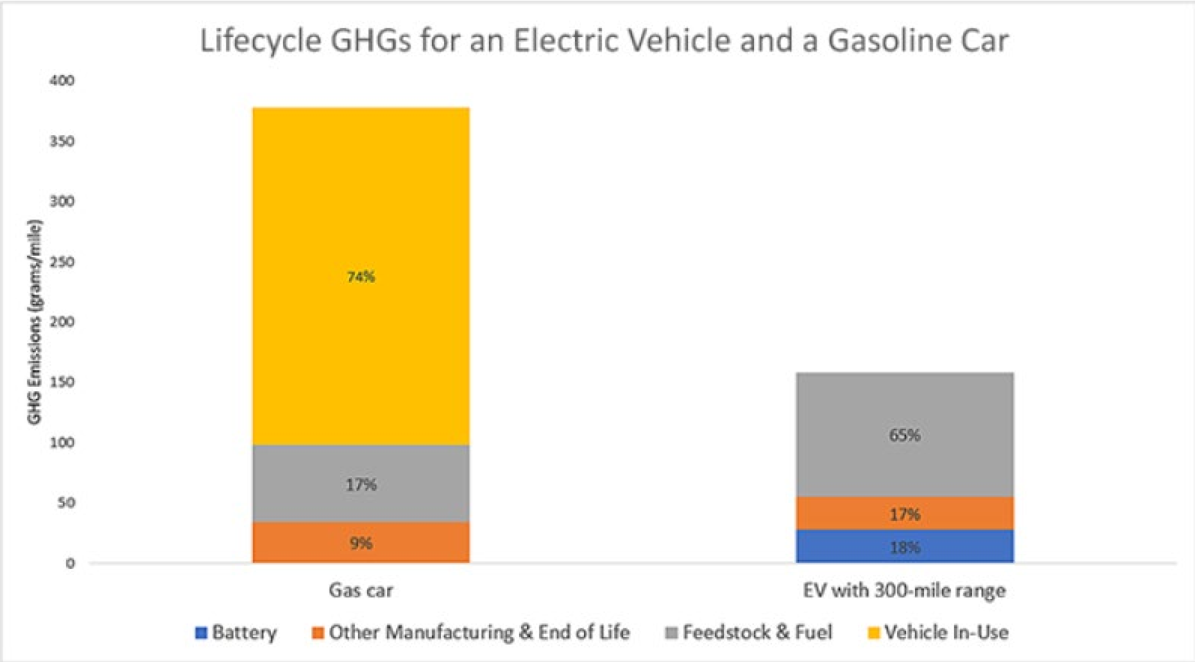

Figure 1.1. Lifecycle GHGs for EVs and gasoline cars [6].

Vehicle emissions can be measured in three ways: a tailpipe basis, a well-to-wheel basis, or a cradle-to-grave basis. Tailpipe emissions deriving from the chemical reaction of the fuel used in vehicles. Well-to-wheel emissions consist of tailpipe emissions, as well as emissions from the fuel or electricity generation and distribution stages. Cradle-to-grave emissions, on the other hand, include well-to-wheel emissions, such as material and vehicle production, end-of-life, recycling, and scrapping. Conventional vehicles with an ICE generate direct tailpipe emissions. Well-to-wheel emissions encloses all tailpipe emissions. Moreover, it includes the extraction, refining, and processing of fuel and its distribution to petrol stations and usage in conventional vehicles, and for EVs, the extraction of resources required for the production of electricity, the generation and distribution of electricity at power plants and the use of vehicles at charging stations. Cradle-to-grave emissions include all assessed emissions from well-to-wheel, as well as emissions affiliated with the vehicle and battery manufacturing process, recycling, and disposal [7].

Emissions from vehicles cause the release of gases such as CO_2 and methane that trigger GHG effects. With the increase in the amount of CO_2 in the air, there is a significant rise in air pollution, which causes various respiratory diseases such as asthma and pneumonia. For this reason, it is essential to reduce vehicle emissions and measure them at regular intervals. Figure

1.2 shows the annual pounds of CO_2 emissions per vehicle for the year 2022. From the data in Figure 1.2, it is apparent that conventional vehicles produce almost three times as many pounds of well-to-wheel emissions as BEVs. Hybrid vehicles produce slightly more emissions than PHEVS ,yet, this rate is 1.5 times higher than BEVs [6].

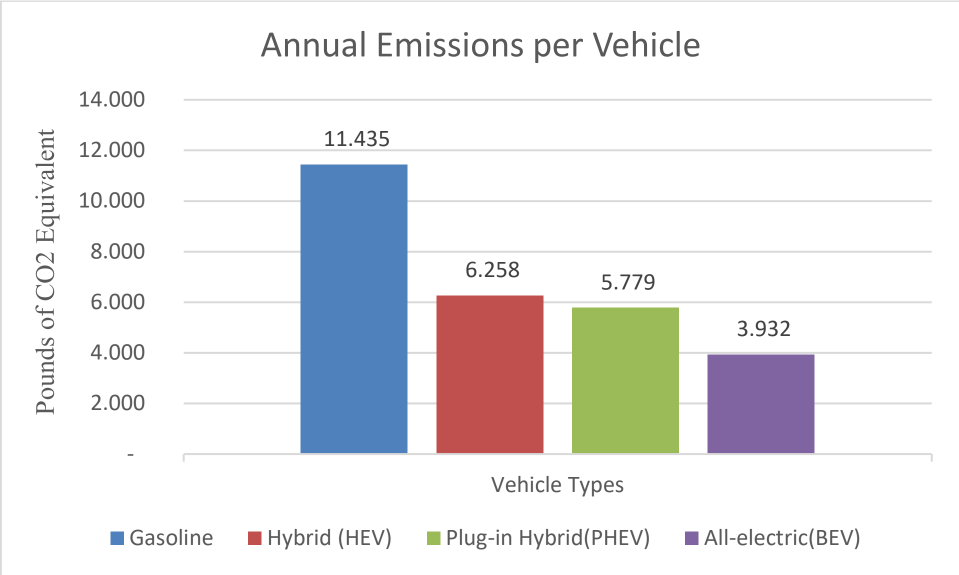

Figure 1.2. Annual pounds of CO2 emissions per vehicle for the year 2022.

1.3. Brief History of Electric Vehicles

The history of EVs is lasting much earlier than internal combustion vehicles. In the early 1800s, there were various attempts by three different people about the production stages of EVs. Thomas Davenport initiated the first EV attempt using two electromagnets, a pivot, and a battery [8]. Scottish Robert Anderson invented the EV between 1832 and 1839. However, it was not preferred because the vehicle's batteries weren't rechargeable. Another Scottish man, Robert Davidson of Aberdeen, invented an electric locomotive in 1837. This locomotive, was demonstrated in 1841, had 6 tons of traction, could go 1.5 miles at 4 mph and again needed new batteries. But the performance of this vehicle, named Galvani, was seen as a threat by the railroad workers and was destroyed [9]. The biggest shortcoming of these inventions was the lack of rechargeable batteries.

With the emergence of rechargeable batteries in 1859, many EV prototypes appeared on the roads in the last quarter of the 1800s and the early 1900s. Electric commercial taxis emerged in New York, with two-thirds of these cars in major cities such as New York, Boston, and Chicago.

The first regenerative braking system, based on the principle of charging the vehicle's battery via braking, emerged in the 1890s [10].

In 1908, an event negatively affected the EVs market. Model T, the first gasoline vehicle to be mass-produced, was introduced by the American engineer Henry Martin Ford. With the mass production of gasoline vehicles, their prices became cheaper, and gasoline vehicles were sold for $ 650. EV sales were at least three times more than gasoline vehicles [8]. In addition, shortcomings such as the short range of EVs, the time required for recharging, and the fact that they are not as fast as gasoline vehicles have reduced the interest in EVs over time.

In the 1960s, EVs came to the fore again with the increased air pollution caused by gasoline vehicles. Besides the Oil Crisis of 1973, the Clean Air Act Amendment of 1990, the enactment of the Energy Policy Act in 1992, and new transportation emission regulations issued by the California Air Resources Board, the process of returning to EVs accelerated. With these developments, automobile manufacturers began to modify some of their popular vehicle models into EVs [11]. General Motors did not choose to modify its current models to EVs in this process, as other vehicle companies did. General Motors introduced the EV1 model in 1996, launched as the "world's most efficient production vehicle." The vehicle had a range of 80 miles and could go from 0 to 50 miles in just seven seconds. It created a considerable sensation at the time. However, due to high production costs and commercial marketing failures, GM stopped production of EV1 in 2001.

It wasn't until the beginning of the 21st century that EVs truly became a trending topic. An important milestone was the invention of the Toyota Prius, launched in Japan in 1997. In the first year when it was produced, the world's first mass-produced HEV, Toyota Prius, sold about 70,000 units. Since then, increased petrol costs and legislation to cut carbon emissions have made the Prius the most popular hybrid vehicle globally during the past ten years. Not lately, major automobile manufacturers such as Honda, Nissan, Chevy, and General Motors have also started to produce EVs.

Since 2008, with a launching model known as Roadster coined by Tesla Motors, EVs technology has experienced a golden age. Tesla was the first company to utilize lithium-ion batteries. Before long, a driving range reached more than 200 miles. This development revolutionized the automotive market. Later, the Tesla Model S series, introduced in 2012 for luxury cars, made EVs more attractive. By 2017, versions of the Model S could travel more than 300 miles on one charge. The 2022 model Tesla Model S plaid series allows driving up to 396 miles (637 km). When it comes to the most extended mile range, Lucid's Air Grand Touring model offers 516 miles (830 km) of driving these days.

Turkey has recently introduced EV technology with the launch of TOGG. The first prototype was produced at the end of 2019 as a concept with an emphasis on domestic and national cars. The vehicle will be produced in five different models and is expected to be produced as a C-SUV in the first stage, as shown in Figure 1.3. Later, C-Hatchback, B-SUV, C-Sedan and C-MPV models will be released, respectively. This vehicle, which has two different engine options, accelerates from 0 to 100 km/h in 7.6 seconds with its 200-horsepower engine and 4.8 seconds with its 400-horsepower engine. This vehicle, which uses lithium batteries, has two options that can go 300 kilometers and 500 km on a single charge. Also, the planned time to charge 80 percent of the battery is less than 30 minutes. The vehicle also has features such as regenerative braking, autonomous driving, remote intervention, and 5G internet technology [12].

Figure 1.3. Turkey’s All-electric vehicle TOGG [12].

1.4. Types of Electric Vehicle

According to their power source, EVs can be classified as HEVs, BEVs, and Fuel Cell Electric Vehicles (FCEVs). HEVs are powered by two different power sources for administering driving power, an ICE and an electric motor, while BEVs are powered by a rechargeable battery and driven by an electric motor. Although they use the same propulsion system as BEVs, FCEVs are pretty different as they generate electrical energy using hydrogen and air through their fuel cells [13].

2. LITERATURE REVIEW

According to switching devices, previous studies on MDIBC topology can be classified into three main groups. The first group uses Si-IGBT or Si-MOSFET semiconductors in the MDIBC topology. As an example of the first group studies, Hegazy proposed IGBT-based MDIBC for EVs and compared the results with BC, IBC, and MDBC. Hegazy analyzed the converters with MATLAB Simulink software. In addition, he built a TMS320F2808 digital signal processor (DSP)-based 30 kW MDIBC prototype in the laboratory environment to verify the analysis results with experiments. According to the simulation and test results, MDIBC has proven its superiority over other converters in terms of efficiency, reliability, and high performance [14]. Priya et al. also examined IGBT-based MDIBC topology and compared it with BC, IBC, and MDIBC using MATLAB Simulink. According to the simulation results, MDIBC performed with greater efficiency and stability. Authors also designed the controllers of the converters using PID controls and investigated the closed-loop responses of converters, and proved that the MDIBC structure reduced the steady-state errors more than the others [15]. Abu Khanipah et al. investigated the MDIBC topology to overcome FCEVs' weak point, such as low output voltage and high input current ripple. Authors compared MDIBC and IBC topologies using MATLAB Simulink. Authors designed the converters with IGBT semiconductors at the conditions of 24 V input voltage, 10 kHz switching frequency, and 0.25 duty cycle. According to the simulation results, while 94% efficiency was obtained with IBC, 97% efficiency was obtained with MDIBC. Besides, passive component size and ripples are also further reduced [16]. R. Seyezhai made a comparison of MDIBC and IBC for FCEVs. The converters were designed at the conditions of 20 kHz switching frequency, 0.45 duty ratio, 24 V input voltage, and power MOSFETs. Results were compared with MATLAB Simulink. MDIBC outperformed the simulation results, and achieved 96.4% efficiency [17]. R. Latha et al. have driven a 4 kW Induction Motor with a 10 kW MDIBC. Authors designed MDIBC with 200-volt input voltage and 400-volt output voltage, 20 kHz switching frequency, and used MOSFET as switching equipment. In order to lessen ripple in the DC link voltage and input inductor current, they adopted a dual loop control approach using a PI controller. MATLAB Simulink was used to carry out both open-loop and closed-loop simulation. Average input current, overshoots in the output voltage, ripple in the input current and steady-state errors have all been shown to decrease in simulations [18].

In the second group, SiC-based MDIBC was searched for. In this group, O. Şen compared the Toyota Prius converter with MDIBC topology in his master's thesis. O. Şen redesigned Prius' Si-based converter operating at 10 kHz switching frequency with MDIBC structure using SiC MOSFETs. He designed MDIBC at the 40 kHz switching frequency, and according to his calculations, MDIBC achieved 98.2% efficiency at 5% input current ripple and 0.5% output voltage ripple conditions [13].

GaN-based MDIBC was recommended as the third group. When the previous studies are investigated, this thesis will be the first study to integrate GaN material into the MDIBC structure. In this study, the Si-IGBT-based Toyota Prius converter operating at 10 kHz switching frequency was redesigned with a GaN-based MDIBC structure at the 100 kHz, 80 kHz, 60 kHz and 40 kHz switching frequencies and these two converters were compared in terms of efficiency, power loss, inductor and capacitor size, current and voltage ripples.

3. DC/DC CONVERTERS IN EV TECHNOLOGY

There have been some promising developments in EV technology, but the field is still maturing. The key impediments to more competition with conventional vehicles and wider acceptance are the cost, capacity, and charging time of the batteries, as well as improved energy performance of the vehicles in general. DC/DC converters are one example of a circuit component that may be optimized to reduce power usage and hence it increases energy efficiency.

3.1. Overview of DC/DC Converters

DC/DC converters are a subgroup of the power converter family and can be defined as circuits that convert one level of voltage to another one. They are commonly applied in electronic devices that have rechargeable batteries [19] in order to regulate voltage as well as raise voltage levels that occur at the battery's output from low to high. In EV technology, where high voltage is highly required, managing power fluctuations is particularly difficult since it decreases the speed, performance, and longevity of the circuitry. Referring to power flow capability, DC/DC converters can be unidirectional and bidirectional, handling energy flow from the source only or both sides to the source, respectively. In the aspect of electronics, the most important difference is that unidirectional DC/DC converters can use diodes to prevent reverse current flow, while in bidirectional DC/DC converters, these diodes are replaced by switching devices to transform them into bidirectional topology [20].

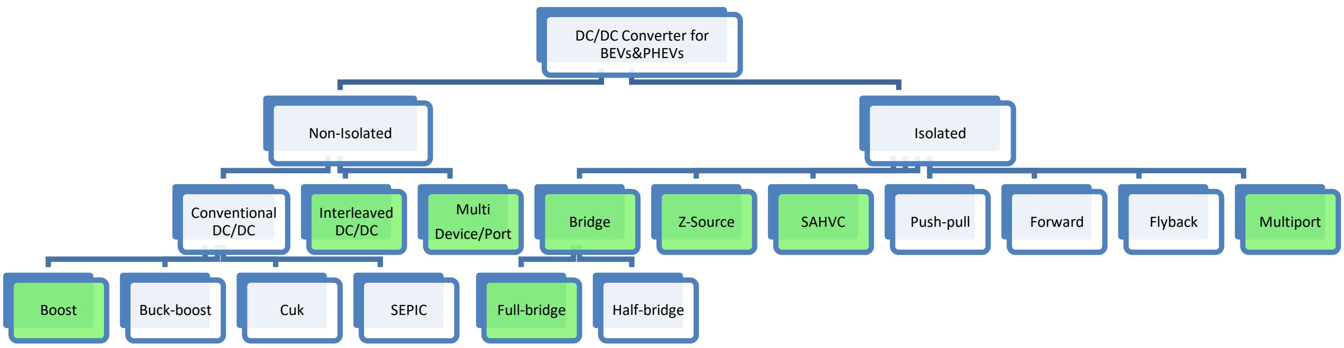

Figure 3.1. DC/DC converter topologies [1].

Market-available DC/DC converters come in more than 500 different configurations [21]. However, most of them fail to meet the needs of EV technology. A classification diagram is in Figure 3.1 outlines DC/DC converter configurations which are appropriate for usage in not only BEV but also PHEV technologies. It is to be noticed that the green colored boxes represent the DC/DC converter's mostly preferred topologies. They are classified according to their power level, the direction of power flow, operating principle, and operating modes into non-isolated and isolated groups [1].

Non-isolated DC/DC converters are preferred in medium and high-power requirement EVs, and they are divided into three groups: conventional, interleaved, and multiport converters. Conventional DC/DC converters may be further to put into Boost, Single-ended primary-inductor converters (SEPIC), Cuk, Buck-boost. EVs with low to medium-power requirements frequently utilize isolated DC/DC converters and they are arranged into seven main groups: Bridge, Z-Source, Sinusoidal amplitude high voltage bus converter (SAHVC), Push-pull, Forward, Flyback, and Multiport.

With respect to topologies, bridge converters may be grouped as Full-bridge and Half-bridge ones. Isolated converters have three-stage DC/AC/DC. Input voltage is stepped up via a high-frequency transformer (HFT) to an intermediate AC stage. These converters are suitable for situations where electrical isolation—complete separation of the input and output sides—is necessary for reliable power transmission with less noise and low electromagnetic interference (EMI) [22]. However, these converters have different shortcomings such as high conduction loss, the requirement for a high number of components, and low efficiency, which are important obstacles to further usage [23].

Regarding to weightiness, efficiency, and power density, non-isolated converters are one step ahead of isolated ones since they do not require transformers that require magnetic coupling. Besides, there are no transformer conversion losses from DC to AC and then back to DC, which is a factor that directly affects efficiency. Additionally, the existence of a transform in the circuit increases EMI and leads to leakage inductance which causes high voltage stress on switching devices and diodes.

The boost converters (BC) are a subgroup of non-isolated converters that are frequently used in circuits requiring higher output voltage levels ranging. In EVs, generally, the output voltage of the batteries is between 180 to 360 V. Boost converters use this battery output voltage as an input and stepped up it between 400 and 750 V for the DC bus voltage [22]. BC consists of**,** at least**,** a semiconductor switch, a diode, and two storage elements a capacitor, and an inductor. Filter-based capacitor reduces output voltage ripples while series connected inductor reduces input current ripples. In terms of EV technology, BC is suited for a wide range of applications because of its various benefits, including ease of provisioning electromagnetic interference needs, simplicity of driving switching components, and low cost. Furthermore, efficiency at full load might reach up to roughly 84% [20]. Despite the low cost, various difficulties must be overcame for EV technology to be widely used. These drawbacks include high input current and output voltage ripples along with large, bulky capacitors and inductors that limit circuit simplification.

Designing multiphase interleaved power stages is one approach to overcome these issues. In multistage power conditions, characteristic of EV's topologies and some other high-voltage/ high-power applications, multistage conversion is highly required. A multistage converter comprises of multiple power stages with parallel inputs, outputs, and shifted driver signals to provide uniform distribution across the switching period [24]. The interleaved boost converter (IBC) structure operates according to the method of connecting multiple boost converters in parallel at the same frequency and driving the switches with a phase shift. The switching pattern is shifted by 360°/n, where n is the number of phases. In this structure, the circuit consists of one switch, one inductance, and one diode per phase, and they are interconnected. In order to maintain a consistent current throughout multiple boost converters, all inductors are similar. According to standard BC, IBC has better qualities with increased effectiveness, smaller size, more dependability, and fewer total harmonic distortions (THD) [25]. With this construction, the current ripple frequency is n times greater than the switching frequency. The structure also enables the current to be divided into two or more pathways help, which in turn reduces conduction losses. It should also be pointed out that the efficiency increases in direct correlation with the number of phases.

On the other hand, a multidevice boost converter (MDBC) has multiple switches, the number of which is nominated by m, connected in parallel to a single inductor. Although the operating principle of the MDBC is the same as BC, the main difference of the MDBC topology is that devices connected in parallel share the input current, providing a more reliable structure. Additionally, compared to conventional boost converters, switching stress voltage is reduced. In addition, compared to a standard BC, the size of the passive components can be decreased by a number of ***m*** thanks to the increased number of switches [15].

MDIBC can be defined as a combination of the multidevice boost converter and interleaved boost converter. Having the advantages of both converter structures, MDIBCs are most prominently used in applications requiring high-power outputs (>10 kW). When compared to the other structures, the current and voltage ripples produced by these structures are significantly lower, while the size and weight of the passive components are also reduced. Besides, these structures offer less levels of electromagnetic interference as well as stress within the switches. By operating the gate signals in an interleaving technique, current is shared between various phases, which helps lowering current ripples [15]. The superiority of this converter over other DC/DC converters is emphasized in terms of efficiency, high performance, and reliability [1, 15, 26]. Yet, this topology contains a large number of components increasing both the conduction and switching power losses. For this reason, the MDIBC converter is frequently not preferred despite its advantages.

3.2. Switching in DC/DC Converter

Refers to switching components for MDIBC topology, the most prominent types of switches are Silicon-based semiconductors such as Silicon Insulated Gate Bipolar Transistors (Si-IGBTs) and Silicon Metal Oxide Semiconductor Field Effect Transistors (Si-MOSFETs). Both Si-IGBTs and Si-MOSFETs are important building blocks of many power electronic applications. When they operate in switching mode, they allow electricity flow in the on-state and stop it in the off-state. Si-IGBTs are extensively used as switching devices in high-power applications with a switching frequency of less than 20 kHz such as in inverter circuits, unregulated power supply (UPS) systems, switch mode power supplies (SMPS), while Si-MOSFETs are used in low-power applications with a switching frequency exceeding 20 kHz such as power supplies, automotive, industrial and communications systems. They are also widely used in low-to-high-voltage applications such as smartphones, computers, led lights, solar, and wind turbines.

Despite the fact that silicon semiconductors have a number of benefits, including high maturity, cost-effectiveness, abundance in nature, and shown durability, silicon's theoretical performance has been almost entirely reached on behalf of its physical features and characteristics. With the development of technology and the widespread use of power electronics semiconductors in EVs, renewable energy systems, and industrial and aerospace applications, the need for devices that have higher switching speeds, lower switching losses, withstand higher temperatures, and reach higher powers has increased [27]. All these developments have revealed the need for a new material to meet the above-mentioned requirements. Therefore, the interest in wide band gap materials (WBGs) has recently stimulated.

WBG devices such as Silicon Carbide (SiC) and Gallium Nitride (GaN) provide many advantages over Silicon-based devices and have been developed to overcome the limits of silicon power semiconductors [28, 29]. GaN and SiC-based power devices such as SiC MOSFET and GaN Transistor compete against silicon IGBTs and MOSFETs in various segments. With the help of the properties such as high bandgap, large critical breakdown electric field, large electron velocity and high thermal conductivity of these new semiconductors, the power losses caused by the MDIBC containing many components can be reduced.

Table 3.1 shows that comparison between competing requirements of Si, 4H-SiC (SiC occurs in many different crystal structures, called polytypes, 4H-SiC is referred the hexagonal one) [30] and GaN family of power semiconductor devices, with respect to several parameters, such as band gap, electron mobility, electron saturated velocity, critical breakdown electric field, and thermal conductivity.

Table 3.1. Key electronics parameters of Si, 4H-SiC, and GaN [31].

Property	Si	4H-SiC	GaN
Band gap energy, (Ev)	1.12	3.26	3.43
Breakdown electric field, (kV/cm)	250	2200	3300
Electron saturated velocity, ($x10^7$ cm/s)	1	2	2.5
Thermal conductivity, λ(W/cmK)	1.5	3.0-3.8	1.3/4.1
Electron mobility, (cm^2 / Vs)	1300	950	2000

It can be understood from Table 3.1 that concerning with the critical breakdown electric field, GaN shows better performance than Si and SiC. Referring to the critical breakdown of the electric field, GaN is about thirteen times as high as Si and one and half times as high as SiC. This property allows for the design of high-performance power devices, with almost thirteen times thinner and nearly a hundred times higher doped voltage-blocking layers with higher impurity concentrations [27, 32]. For the same operating voltages, GaN requires less space than Si. In other words, GaN can be operated at higher voltages more reliably for the same size. In the case of band gap properties, GaN has a wider band gap than SiC and Si. From this data, we can say that GaN works more reliably than SiC and Si at high voltages and temperatures [33]. WBG devices enable the designer to retain a high switching frequency while maintaining lower switching and conduction losses, achieving smaller inductor and capacitor sizes without an associated rise in switching losses [34, 35]. In that case, higher electron mobility and electron saturation velocity properties allow for a higher frequency of operation [36].GaN has superiority over SiC and Si. In terms of thermal conductivity, SiC has better performance than GaN and Si. This makes SiC suitable for high-temperature applications. GaN has a lower thermal conductivity than Si. But, GaN's high efficiency diminishes the thermal loads caused by the circuit, allowing for a colder operating temperature than silicon. This results in improved thermal management and minimizes the need for an external heatsink.

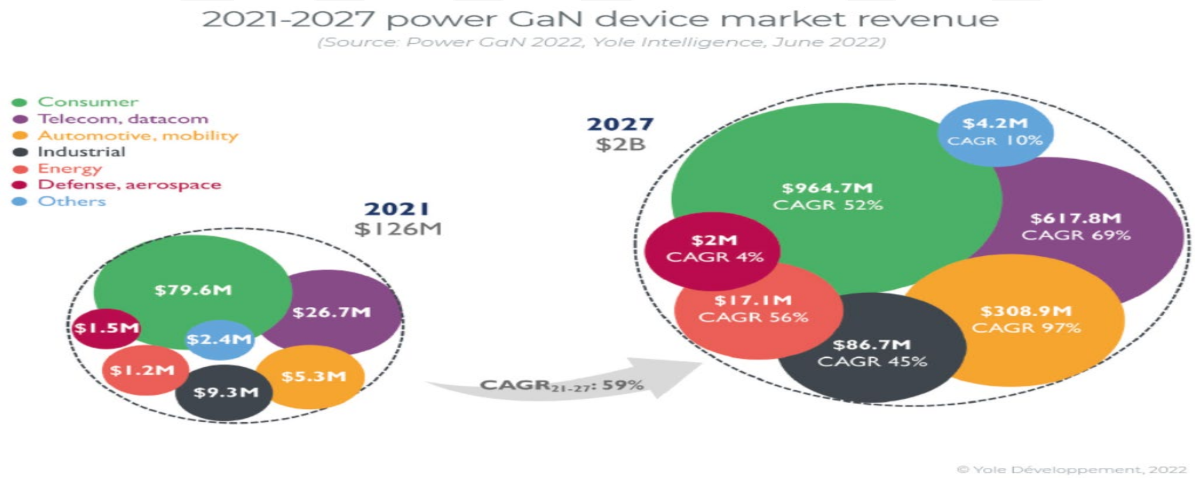

Figure 3.2. 2021-2027 power GaN device market revenue [37].

The acceptance of GaN-based devices has grown significantly during the past ten years and GaN converters are no exception. Primarily due to the expanding market share, the design of converters has become a popular topic for the scientific community. Figure 3.2 shows that according to the market research and strategy consulting company Yole Developpement (Yole), the GaN market is expected to be worth US$2 billion in 2027. It was $126M in 2021. Yole also claims that the GaN market automotive DC/DC converters and On-Board Chargers (OBCs) will be a part of the next phase of growth during the estimated time frame, and The GaN automotive market is projected to surpass $227M by 2027, with a Compound Annual Growth Rate(CAGR)2021-2027 of 99% [37].

In this study, we first investigated a Si IGBT-based converter, which is used in Toyota 2010 Prius (3rd Generation) vehicle. The converter is obtained with respect to power efficiency, current, and voltage ripple factor. After that, the circuit was reconstructed by MDIBC topology with All-SiC and All-GaN semiconductors, respectively. Both topologies were also investigated with respect to the same parameters. All parameters were calculated with the help of PSpice simulation software. In the end, comparing all obtained results, we discussed the pros and cons of All-GaN MDIBC, All-SiC MDIBC, and Si-based converter topologies.

4. OPERATING PRINCIPLE OF BC AND MDIBC

The mode of operation of the converter is determined by the method of which energy stored in the inductor is transferred to the output, during the ON and OFF states of the switching equipment. If the energy stored in the inductor is completely discharged and goes zero during the switching time, it is called discontinuous conduction mode (DCM); if not, it is called continuous conduction mode (CCM). Gate signals control active switching elements, and they are turned ON and OFF by the pulse-width modulation (PWM) technique [38]. The period in which the pulse signal is active during a switching period is called the duty cycle. The desired output voltage value in converters can be determined with the duty cycle. Depending on the type of converter topology, the output voltage value can be directly or inversely proportional to the duty cycle [13].

4.1. Operating Principle of Standard Boost Converter

The operating principle of a boost converter is based on the principle of increasing or decreasing the magnetically stored energy on the inductor using switching elements [39]. Figure 4.1 shows the operating principle of the switching element in the ON state (Switch is closed). With the pulse applied to the gate signal of the switching element, the switch is in the ON state, and current i_L passes from the positive terminal to the negative terminal on L, which stores energy in its magnetic field. Since the switching element is in the short circuit position, the current does not pass through the remaining elements of the circuit, D_2, Co, and load V_{out}, so the circuit completes itself through the switching equipment [40]. The voltage that flows the inductor V_L is just the input voltage V_{in} so V_L=V_{in} [41].

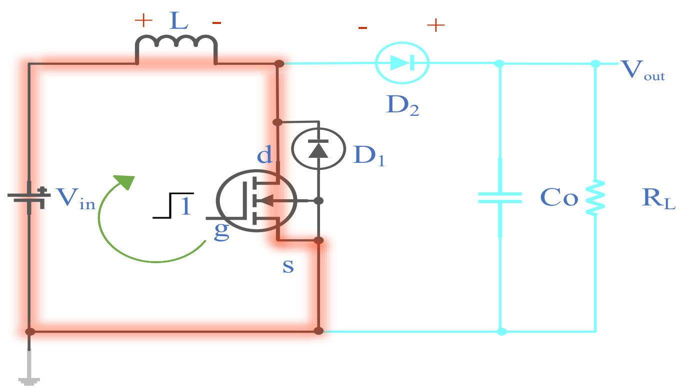

Figure 4.1. Boost converter operation at ON state.

Figure 4.2 shows the path of the current when the switching element is in the OFF state (Switch is open). When the switch is OFF state, the impedance will start to rise and the current will decrease. This sudden decrease in the current will create a back electromagnetic field (e.m.f) on the inductor and the polarity of the inductor will change to keep the current flowing from the left side to be minus and the right side to be positive. This will create a higher voltage source with V_{in} and back e.m.f.(V_L) across L connected in series in the circuit. This voltage (V_{in}+V_L) will pass through the diode D_2, charge the Co and supply the load. Thus, a higher output voltage is obtained compared to the input voltage.

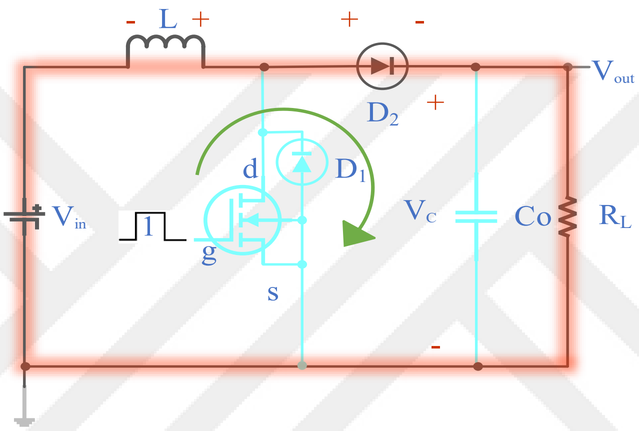

Figure 4.2. Boost converter operation at OFF state.

Figure 4.3 shows the operating principle of the switching element when it switches from the OFF state to the ON state again after the first start-up. The V_{in}+V_L voltage formed on the capacitor is discharged onto the load. In this process, since the cathode terminal of the diode is more positive than the anode terminal, and it prevents the discharge of the capacitor onto the switching equipment. The critical thing in this process is that the switching equipment must return to the OFF state quickly enough without completely discharging the capacitor. Thus, the desired constant output voltage level is obtained on the output.

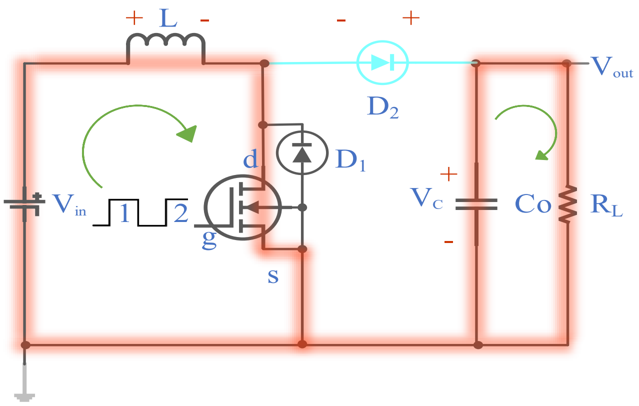

Figure 4.3. Boost converter operation when the second time at ON state.

In steady-state operation, the current flowing out through the inductor must be equal to the current flowing in through the inductor so that the net change of the inductor current over any one complete switch cycle is zero [41]. Assuming that there is steady-state operation, all the components are ideal, duty cycle (D) is the same for all switching devices, and the converter is operating in CCM mode, the equations are as described below.

When the switch is ON state for a time, this situation is called T_{ON}, and when the switch is OFF state for a time and this situation is called T_{OFF}, So period T will be,

$$T = T_{ON} + T_{OFF} \tag{4.1}$$

The duty cycle D is,

$$D = \frac{T_{ON}}{T} \tag{4.2}$$

When applying Kirchhoff's voltage law (KVL) to Figure 4.1, the obtained formulas are shown below [42]. Since the input current ripple of the converter (Δi_n) equals to inductor current ripple (Δi_L), Δi_n and Δi_L are equal to each other.

$$V_{in} = V_L \tag{4.3}$$

$$V_L = L\frac{di_L}{dt} = V_{in} \tag{4.4}$$

$$\frac{di_L}{dt} = \frac{\Delta i_L}{\Delta t} = \frac{\Delta i_L}{DT} = \frac{V_{in}}{L} \tag{4.5}$$

$$\Delta i_L(ON\ state) = \Delta i_n = \frac{V_{in}}{L} DT \tag{4.6}$$

When applying Kirchhoff's voltage law (KVL) to Figure 4.2,

$$V_{in} = V_L + V_O \tag{4.7}$$

$$V_L = L\frac{di_L}{dt} = V_{in} - V_O \tag{4.8}$$

$$\frac{di_L}{dt} = \frac{\Delta i_L}{\Delta t} = \frac{\Delta i_L}{(1-D)T} = \frac{V_{in} - V_O}{L} \tag{4.9}$$

$$\Delta i_L(OFF\ state) = \left(\frac{V_{in} - V_O}{L}\right)(1-D)T \tag{4.10}$$

Since T_{OFF}= T $-T_{ON}$= $T - DT$ =$(1-D)T$, so we can say Δt =$(1-D)T$.

In a steady state, since the inductor current during each complete cycle is zero,

$$\Delta i_L(ON\ state) + \Delta i_L(OFF\ state) = 0 \tag{4.11}$$

$$\frac{V_{in}}{L} DT + \left(\frac{V_{in} - V_O}{L}\right)(1-D)T = 0 \tag{4.12}$$

$$\frac{V_O}{V_{in}} = \frac{1}{1-D} \tag{4.13}$$

The current gains are obtained as in Equation 4.14.

$$\frac{I_{in}}{I_{out}} = \frac{1}{1 - D} \tag{4.14}$$

I_{in}, I_{out} are input/output currents, respectively.

The voltage ripple on the capacitor can be found by calculating the variation of the charge (ΔQ) on it. Thus, the converter's output voltage ripple is found in Equation 4.18.

$$\Delta v = \frac{\Delta Q}{C} \tag{4.15}$$

$$\Delta Q = \int i \, dt \tag{4.16}$$

$$\Delta Q = \frac{1}{2}(1 - D)T\Delta i_L + (1 - D)T\left(i_{in} - \frac{\Delta i_L}{2} - i_{out}\right) \tag{4.17}$$

$$\Delta v_{out} = \frac{i_{out}D}{Cf} \tag{4.18}$$

where f is the switching frequency.

Inductance and capacitance values can be obtained using Equations 4.19 and 4.20.

$$L = \frac{V_{in}D}{\Delta i_L f} \tag{4.19}$$

$$C = \frac{i_{out}D}{\Delta v_{out} f} \tag{4.20}$$

When the switch is OFF state, the peak voltage stress on the switch is equal to the output voltage according to Equation 4.21, so this determines the limits of the switching component.

$$V_{sw-peak} = V_o \tag{4.21}$$

4.2. Operating Principle of Multidevice Interleaved Boost Converter

The circuitry design of the MDIBC comprises interleaved two phases, and each phase consists of two switches and two diodes connected in parallel. Figure 4.4 shows a non-isolated unidirectional MDIBC structure [15].

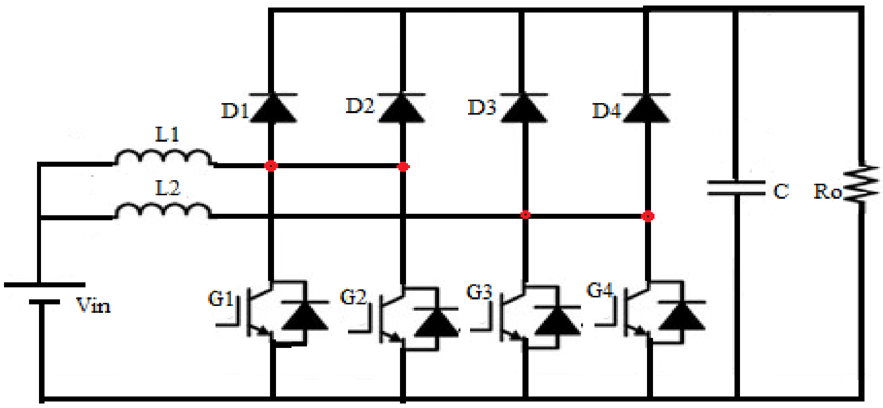

Figure 4.4. The circuitry design of the non-isolated unidirectional MDIBC structure.

There are n phases and m parallel power switches per phase in this structure; the interleaved control shifts the switching pattern by 360°/(***n***x***m***). In this MDIBC design, m is selected to be two, and the value of n is also two. The inductor current's ripple frequency will be doubled with this control method while maintaining the same frequency. This provides higher system bandwidth, which reduces passive components by 4 times when compared to BC and 2 times when compared to MDBC and IBC at the same frequency and ripple values [15]. Passive component miniaturization is advantageous since it allows the converter to have a smaller area and less weight. This also results in a higher converter power density and more compact structure.

In order to achieve a doubled current ripple in the current passing through the inductor at the same switching frequency and to enable interleaved control between the inductors, the driving gate signals' sequence is crucial. In Figure 4.5, the driving gate signals are shown in order at various duty cycles. Figure 4.5 (a) shows the driving gate signals when the duty ratio is 0.25 and when the duty ratio exceeds 0.25, the driving gate signals are depicted in Figure 4.5 (b).

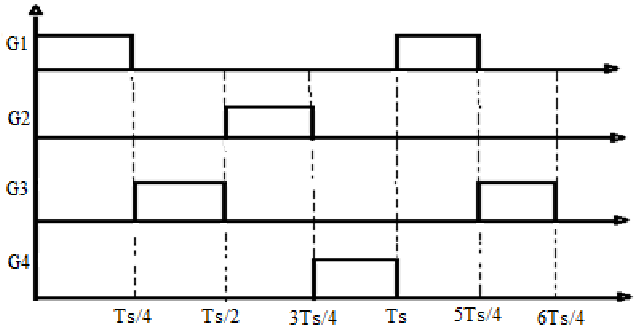

(a) $d = Ts/4$

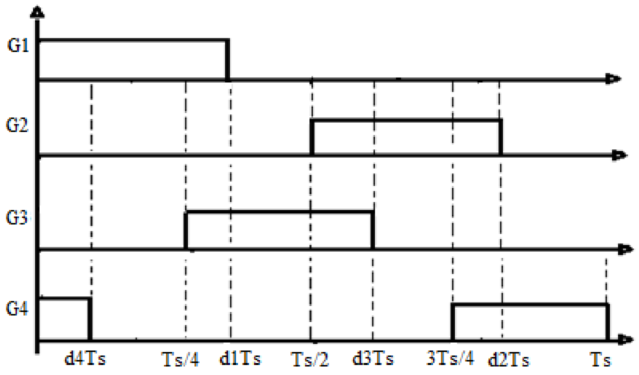

$(b)\ d \geq Ts/4$

Figure 4.5. Switches are driven by gate signals in the following sequence: (a) $d = Ts/4$ (b) $d \geq Ts/4$.

Figure 4.6 shows that the equivalent circuits of the MDIBC structure when the duty ratio exceeds 0.25 [14].

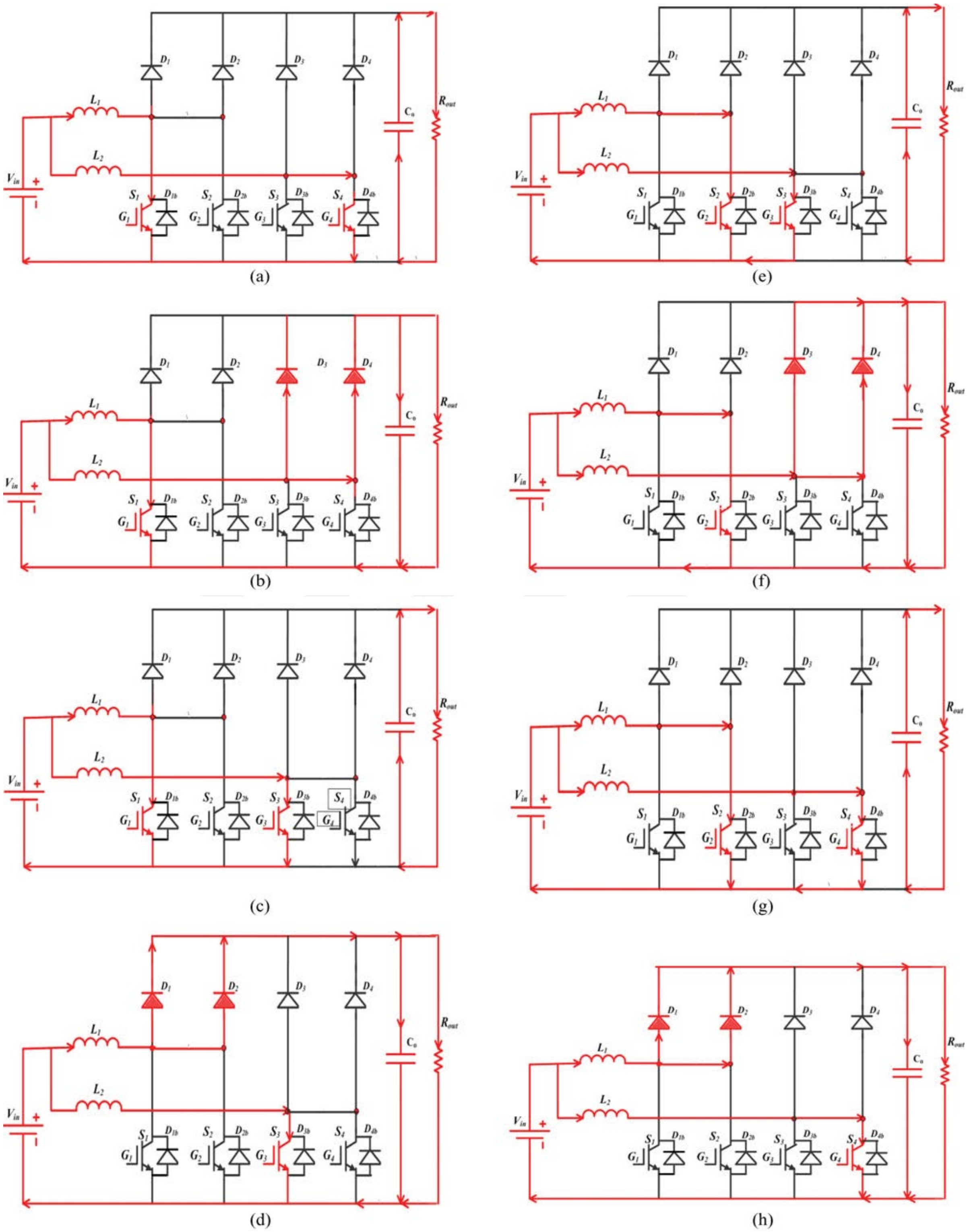

Figure 4.6. Equivalent circuits of the MDIBC structure if the duty cycle is more than 0.25. (a) Phase 1: $0 \leq t \leq d4Ts$. (b) Phase 2: $d4Ts \leq t \leq Ts/4$. (c) Phase 3: $Ts/4 \leq t \leq d1Ts$. (d) Phase 4: $d1Ts \leq t \leq Ts/2$. (e) Phase 5: $Ts/2 \leq t \leq d3Ts$. (f) Phase 6: $d3Ts \leq t \leq 3Ts/4$. (g) Phase 7: $3Ts/4 \leq t \leq d2Ts$. (h) Phase 8: $d2Ts \leq t \leq Ts$.

Assuming that all the components are ideal, the converter is operating in CCM, and all switches have the same duty cycle, the voltage and current gains are obtained as in Equations 4.22 and 4.23.

$$\frac{V_O}{V_{in}} = \frac{1}{1 - mD} \tag{4.22}$$

$$\frac{i_{in}}{i_{out}} = \frac{1}{1 - mD} \tag{4.23}$$

V_O, V_{in}, output and input voltages, i_{in}, i_{out} input and output currents of the proposed converter, respectively. The value of mD must be less than 1.

The inductor and capacitor values of the proposed converter is given in Equations 4.24 and 4.25 respectively.

$$L = \frac{V_{in}\mathrm{D}}{mnf\Delta_i} \tag{4.24}$$

$$C = \frac{i_{out}\mathrm{D}}{mnf\Delta_v} \tag{4.25}$$

Δi and Δv values refer to current and voltage ripples respectively.

5. COMPARATIVE ANALYSIS OF PROPOSED CONVERTER TOPOLOGY

5.1. Analysis of Si-IGBT-based Toyota Prius

The 2010 Toyota Prius model which is the 3rd Generation of the series that started production in 1997 is shown in Figure 5.1. According to [43], since the first Prius model was produced in 1997, Toyota has sold more than 15 million HEVs globally, preventing the emission of more than 118 million tons of CO_2. It combines a 36-hp (27-kW) battery cell with a 98-hp (73-kW) ICE to produce a total net output of 134 hp [44].

Figure 5.1. 2010 Toyota Prius HEV.

According to [45], nickel-metal hydride battery packs are made up of 168 series cells with a 6.5 amp-hour capacity and 1.2 Volts, resulting in a battery pack that generates a voltage of 201.6. Additionally, because the battery pack is only rated for 27 kW, it is expected that the Prius' DC/DC converter can't operate at power ratings beyond 27 kW [44]. The voltage is stepped up from the battery voltage of 201.6 Vdc to 650 Vdc, which is the output voltage of the Prius converter. This voltage is supplied directly to the DC link of the power control unit(PCU) and from this part, power is transferred to the inverter and motor. The circuit diagram for the 2010 Prius PCU is seen in Figure 5.2. [44].

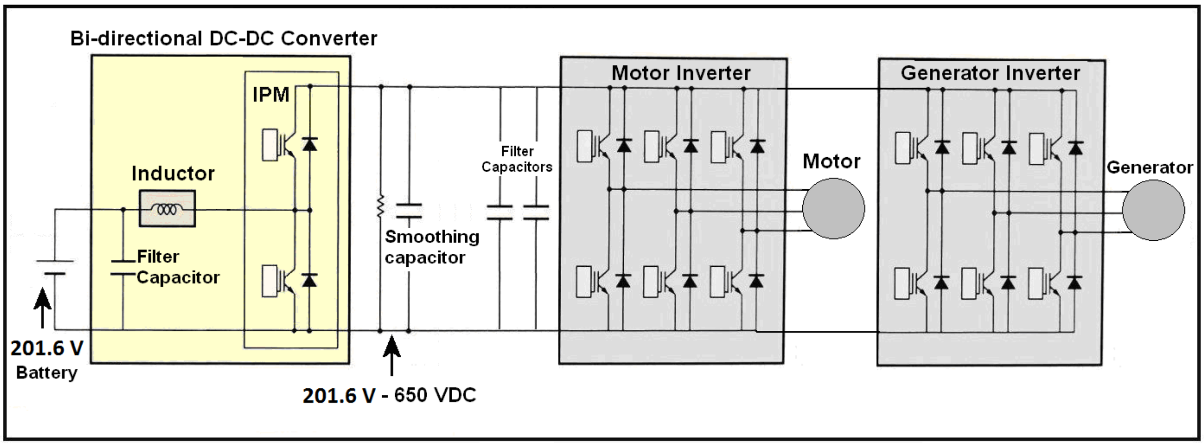

Figure 5.2. Schematic for the PCU of the 2010 Prius.

The bidirectional DC/DC converter of the 2010 Prius consists of a total of four IGBT and four antiparallel diodes. The three of which are connected parallel as a lower switch, operate at frequencies of 5 or 10 kHz with a varying duty cycle to charge and discharge an inductor. When the duty cycle is changed, the inductor's output voltage changes with it. The boost converter power electronics (PEs) are connected to the battery with an inductor of 225.6 µH and a high-voltage (HV) side boost converter with a smoothing capacitor of 888 µF [44]. Figure 5.3. shows the standard unidirectional Si-IGBT-based boost converter of the 2010 Toyota Prius. Q_1, Q_2, and Q_3 represent to Si-IGBT, D_1 is the Si-type diode, V_{DC} is the DC power supply, V_{P1} is the pulse voltage, $L_1$is inductor, C_1 and R_L are the output capacitor and load resistor of the circuit, respectively.

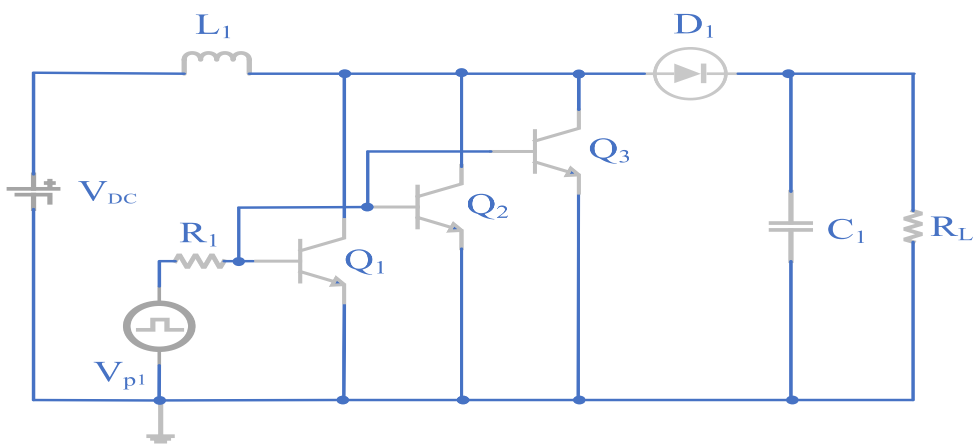

Figure 5.3. Standard unidirectional Si-IGBT-based boost converter of 2010 Toyota Prius.

Assuming that converter is in CCM mode and the switching frequency is 10 kHz, Table 5.1 displays the converter parameters derived from Equations 4.6, 4.13, 4.14, and 4.18.

Table 5.1. Estimated converter parameters.

Parameter	**Value**	**Parameter**	**Value**
Inductor	225.6 µH	Load resistance	15.64 Ω
Output capacitor	888 µF	Duty cycle	0.689
Switching frequency	10 kHz	Input current ripple	61.57 A
Input Voltage	201.6 V	Output voltage ripple	3.23 V
Output Voltage	650 V	Peak Power	27 kW

As the technical properties of the semiconductors used in the 2010 Prius model are not known, semiconductors belonging to that period and being a simulation model were preferred for power loss and efficiency calculations. The main parameters of the selected semiconductors are shown in Table 5.2.

Table 5.2. The main parameters of the preferred semiconductors.

Semiconductor Type	Si-IGBT	Semiconductor Type	Automotive Ultrafast Si-Diode
Manufacturer	Infineon	Manufacturer	STMicroelectronics
Model	IRGPS60B120KD	Model	STTH6010-Y
V_{CES}	1200 V	V_{RRM}	1000 V
I_{CE}	60 A	$I_{F(AV)}$	60 A
V_{GE}	15 V	$V_{F\ (Typ)}$	1.3 V
$T_{j\ (max.)}$	150 °C	$T_{j\ (max.)}$	175 °C

V_{CES}= Collector-to-Emitter Voltage, I_{CE}=Collector-to-Emitter Current, V_{GE}=Gate-to-Emitter Voltage, $T_{j\ (max.)}$= Maximum junction temperature, V_{RRM}= Repetitive peak reverse voltage, $I_{F(AV)}$ = Average forward current, $V_{F\ (Typ)}$= Forward voltage drop.

Since the STTH6010-Y model which is referred as D_1 in the Figure 5.3, is not in the PSpice simulation software's library, the simulation model provided by STMicroelectronics was used [46]. When the converter circuit is simulated, current and voltage ripples are depicted in Figure 5.4. The simulation results confirm that the current and voltage ripple values meet the design requirement in Table 5.1.

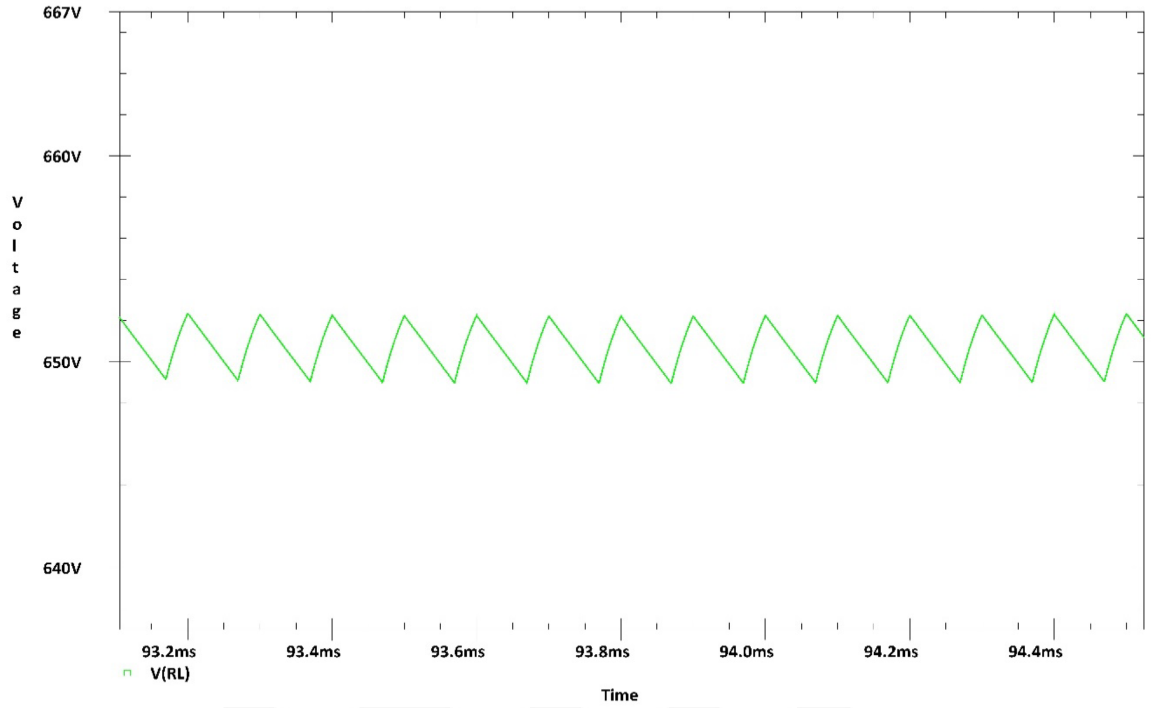

(a)

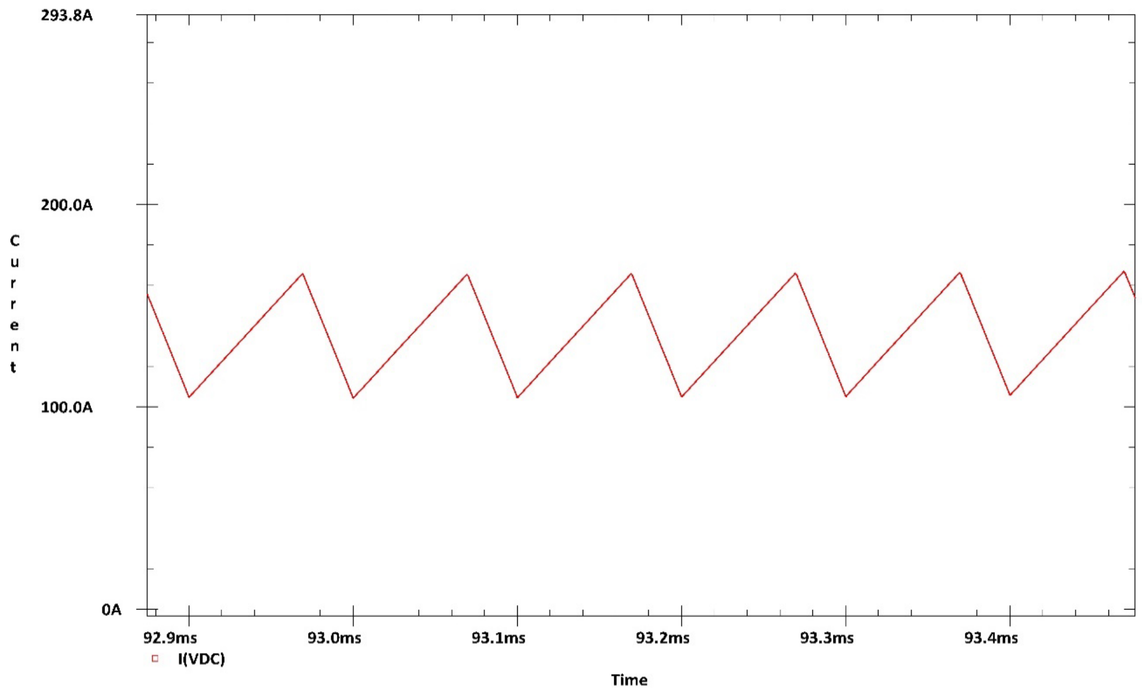

(b)

Figure 5.4. Ripple waveforms of Si-IGBT-based BC in terms of (a) Output voltage ripple. (b) Input current ripple.

Equation 5.1 is used for calculating how much power is lost during conduction in a Si-IGBT semiconductor.

$$P_{cond\_loss}= V_{CE_{(ON)}} I_{C\,(avr)} \qquad (5.1)$$

$V_{CE_{(ON)}}$ is collector-to-emitter saturation voltage which is determined from the IRGPS60B120KD datasheet, while $I_{C\,(avr)}$ is the average value of the continuous collector current. Figure 5.5. shows the current waveform of each Si-IGBT. For the average continuous collector current calculation, the total area of the waveform in a period is considered. According to the graph, it is seen that the ($I_{C\,(avr)}$) value of each IGBT is approximately 31 A.

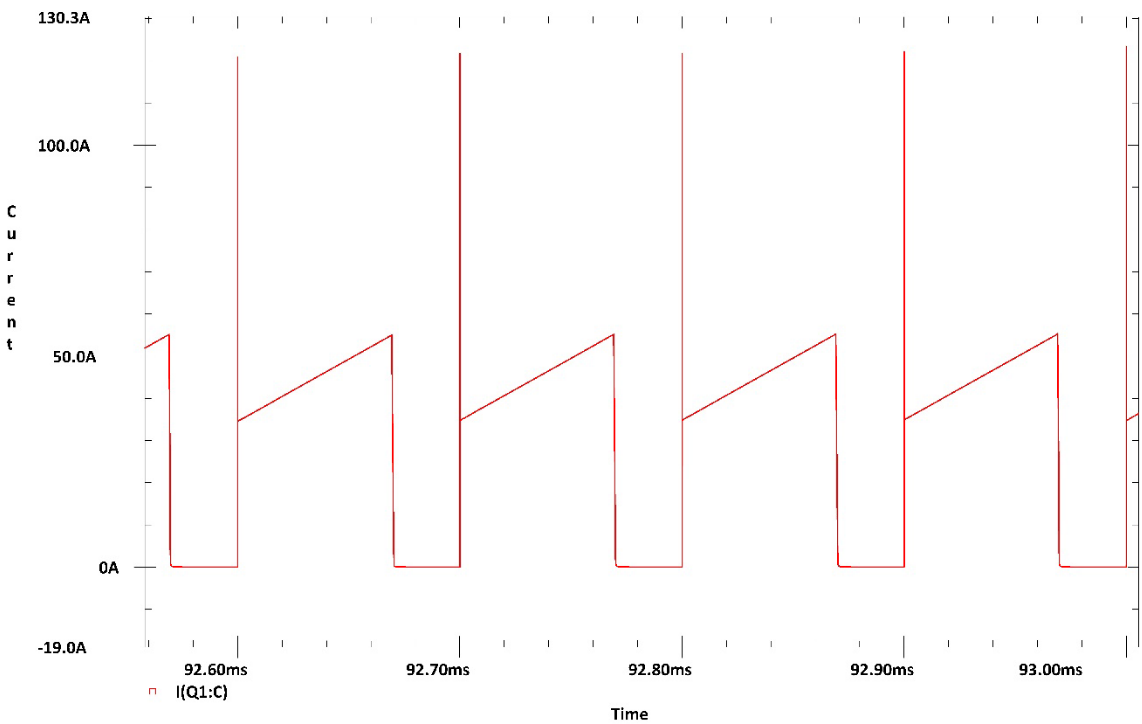

Figure 5.5. The current waveform of Si-IGBT.

Power electronics components are placed under the hood close to the engine for reliable operation in automotive applications. Placing them away from the engine, for example under the rear seat, and connecting them with long cables and connectors can result with unsafe operation. Since the operating temperature of the engine can vary from 105 °C to 140 °C, it is considered that the power electronics circuit elements will operate at 125 °C [38]. Therefore, the ($V_{CE_{(ON)}}$) value must be determined at T_j 125 °C. According to the datasheet of IRGPS60B120KD in Figure 5.6., the $V_{CE_{(ON)}}$ value is approximately equal to 2.3 V under the condition V_{GE}=15 V and T_j = 125°C. According to Equation 5.1, the conduction power loss of each IGBT is 71.3 W. Since there are 3 IGBTs in the circuit, the total conduction power loss is 213.9 W.

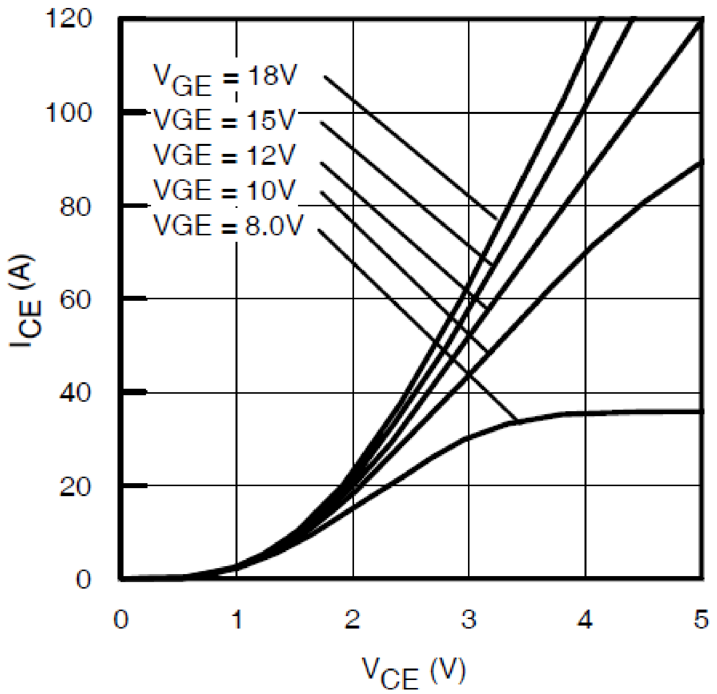

Figure 5.6. The output characteristics of Si-IGBT at 125°C when VGE=15 V [47].

Equation 5.2 is used to determine the Si-IGBT semiconductor's switching power loss.

$$P_{swloss} = (E_{ON} + E_{OFF})f_{sw} \tag{5.2}$$

E_{ON} and E_{OFF} values represent Turn-On and Turn-Off switching losses, respectively. f_{sw} refers to switching frequency. According to the datasheet of IRGPS60B120KD in Figure 5.7., the total energy loss is approximately 7500 µJ. Since the f_{sw} value is 10 kHz, the switching power loss of each IGBT is 95 W. Total switching power loss is 285 W.

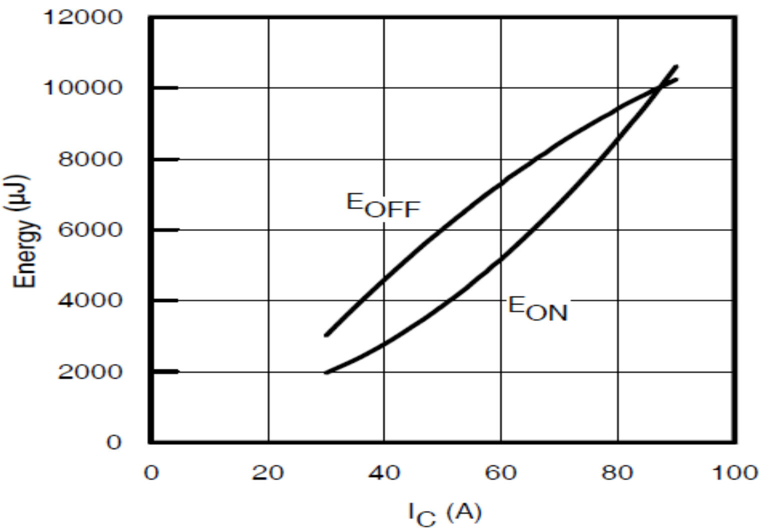

Figure 5.7. Energy Loss vs. IC under the condition TJ=125°C; VCE=600V; RG=4.7Ω; VGE=15V [47].

Equation 5.3 is used to calculate the Si diode's conduction power loss.

$$P_{dcondloss} = V_F I_{F(avr)} \tag{5.3}$$

Where V_F is the forward voltage drop and $I_{F(avr)}$ is the average forward current. Figure 5.8. shows the current waveform of the Si diode. According to the waveform, the average current value is approximately 41.1 A.

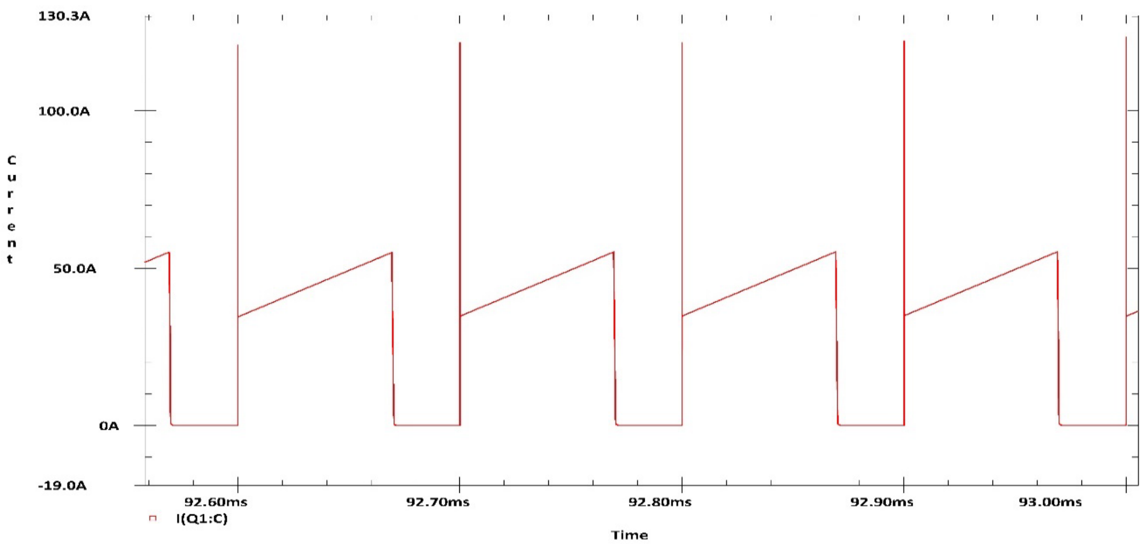

Figure 5.8. The current waveform of Si diode.

Figure 5.9. shows the V_F versus the forward current graph. According to the graph, V_F value is approximately 1.25 V at 125°C. So total conduction loss of the Si diode is 51,375 W.

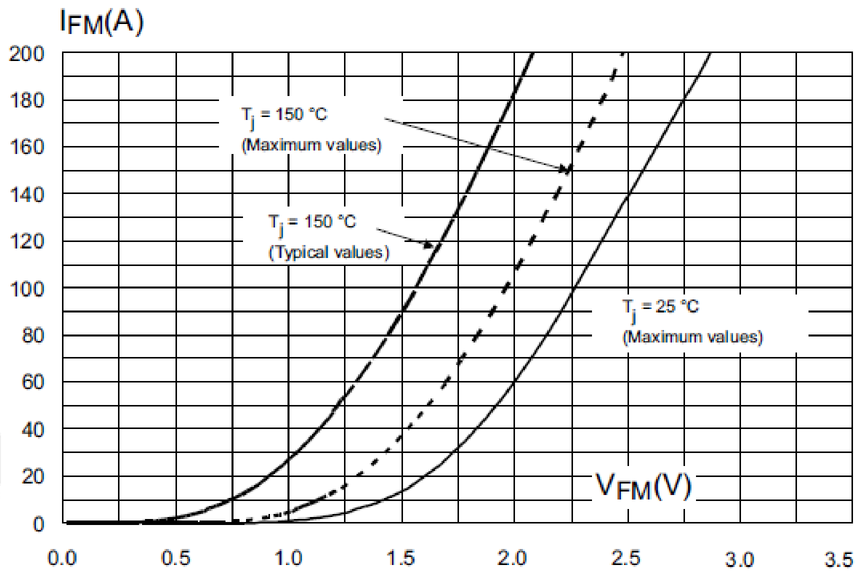

Figure 5.9. The forward voltage drop versus forward current graph [48].

Using Equation 5.4, the Si diode's switching power loss is determined.

$$P_{dsw\_loss} = V_r Q_{rr} f_{sw} \tag{5.4}$$

Since the reverse voltage on the diode (V_r) will be equal to the output voltage, V_r value will be equal to 650 V. The reverse recovery charge (Q_{rr}) value is calculated according to Figure 5.10.

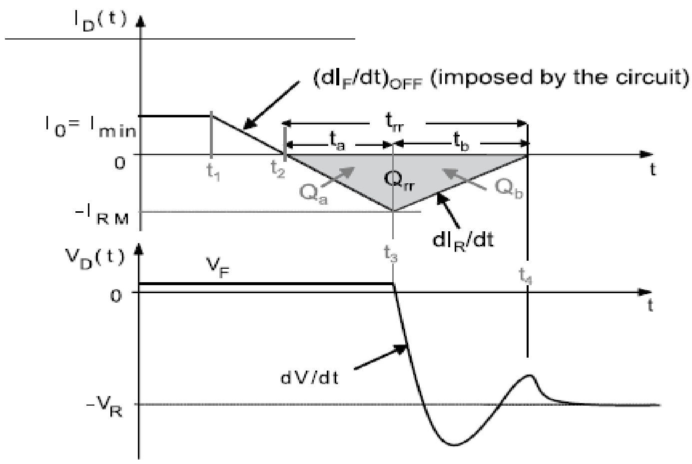

Figure 5.10. Voltage and current waveform of a diode at its turn-off phase [49].

The simulation graph of the diode's switch from forward to reverse conduction is shown in Figure 5.11.

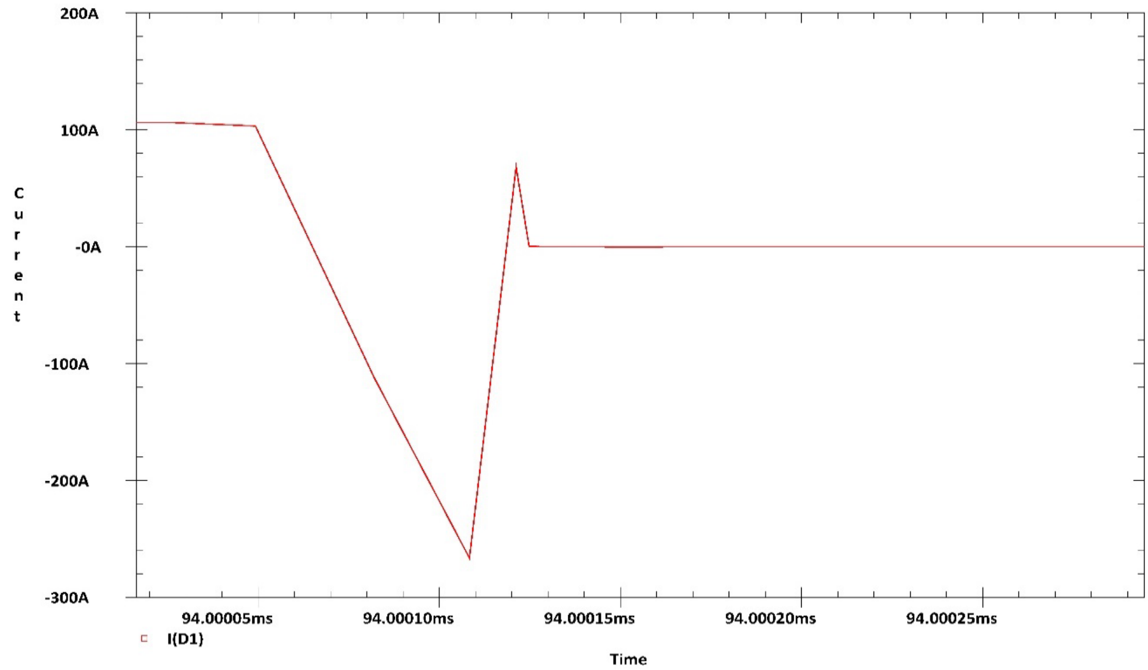

Figure 5.11. The switching from forward to reverse conduction in the diode.

Figure 5.12. shows that reverse recovery charges versus dl$_F$/dt graph under the condition T$_j$ =125°C and V_r =600 V. Using Figures 5.10, 5.11, and 5.12, Q_{rr} value is calculated as approximately 7.4 µC. With the obtained values, the switching power loss of the diode becomes 48.1 W.

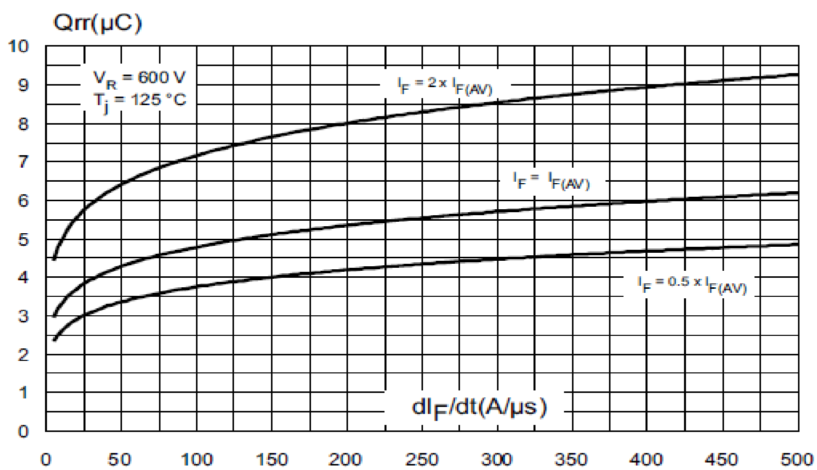

Figure 5.12. The reverse recovery charges versus dlF/dt graph under the condition Tj =125°C and V_r =600 V [48].

The inductor designer application of Micrometals company was used to calculate inductor losses [50]. The part number, shape, and stack information of the inductor were obtained from [45]. Calculated values are obtained at 40°C ambient temperature with the 85°C maximum temperature rise. Table 5.3. shows the inductor design parameters and losses.

Table 5.3. Inductor design parameters and losses.

Parameters	Inductance
Manufacturer	Micrometals
Part Number	T650-2
Stack	5
Shape	Toroid
Inductance Value	225,6 µH
Frequency	10 kHz
Core loss	33.41 W
Conductor loss	101.6 W
Total loss	135 W

Figure 5.13 displays the total power losses resulting from the converter's components. The total conduction loss and switching loss of Si-IGBT are 498.9 W. The total power dissipated by the diode due to its conduction and switching losses is 99.475 W. The power loss consumed by the inductor is 135 watts. The total power dissipation consumed by the converter is 733.375 W.

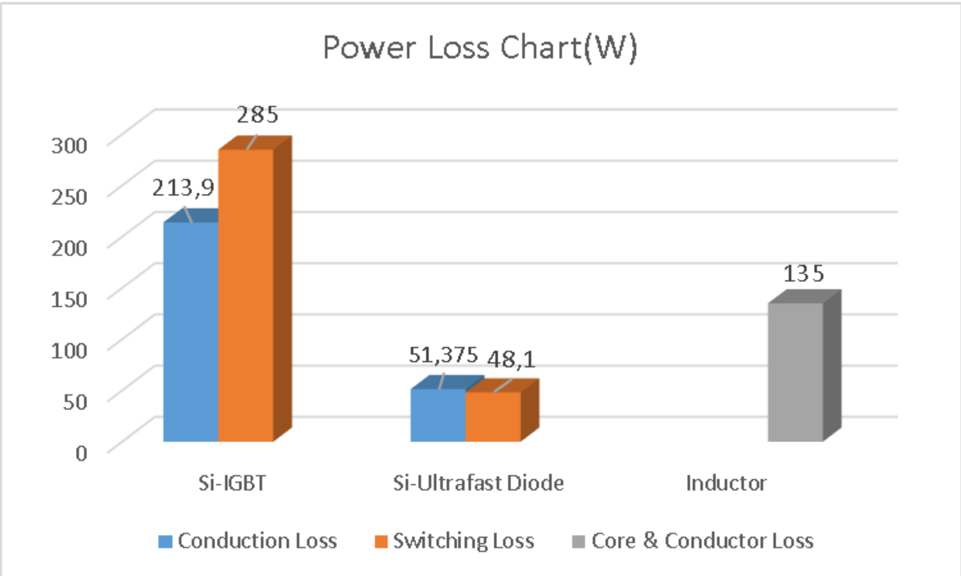

Figure 5.13. Power loss comparison of the components.

The converter's efficiency can be calculated using Equation 5.5. With a 27 kW converter, the system performs at a 97.28% efficiency at 125°C.

$$\eta = \frac{P_{total} - P_{losses}}{Ptotal} \tag{5.5}$$

5.2. Analysis of SiC-based MDIBC

Battery temperature rises as a result of the high current ripple pulled from the battery, which reduces the battery's lifespan. Also, high levels of current ripple decrease conversion efficiency [51]. Besides, a high voltage ripple raises maintenance expenses and reduces the lifespan of the inverter. Due to the advantages of MDIBC topology and superior properties of SiC semiconductors, although the current and voltage ripple levels were further decreased, the inductor and the capacitor sizes didn't exceed the inductor and the capacitor sizes of the benchmark converter. In this study, SiC-based MDIBC is designed for switching frequencies of 40 kHz, 60 kHz, 80 kHz, and 100 kHz. Due to the effects of the current and voltage ripples on the converter, the converter was analyzed in two stages.

In the first stage, the above-mentioned benefits of having low ripple levels were analyzed. As mentioned before, in order to reduce the ripple levels, it is necessary to increase the inductor and the capacitor size and switching frequency. Therefore, at the switching frequency, which has the highest inductor and capacitor size (40 kHz), minimum ripple levels have been calculated that will not exceed the inductor and capacitor sizes of the benchmark converter. Accordingly, 3% current ripple and 0.3% voltage ripple values were determined. In addition, efficiency analysis was performed according to the change in switching frequency at the determined ripple levels.

In the second stage, the current ripple was increased in order to reduce further the size of the inductor, which is the bulky component in the converter, thus, the efficiency of the system was improved. Therefore, 10% current ripple and 0.3% voltage ripple were determined. In both stages, ripple levels were kept lower than the converter of the Toyota Prius, and inductor and capacitor sizes were reduced. In order to compare the designed SiC-based MDIBC with the converter of Toyota Prius, the input voltage, output voltage, and power must be the same. Other design parameters were calculated using Equations 4.22., 4.23., 4.24., and 4.25. Table 5.4. shows the SiC-based MDIBC topology at 100 kHz designed according to the first stage (Δ_i= 3% and Δ_v = 0.3%).

Table 5.4. SiC-based MDIBC parameters at 100 kHz with Δ_i= 3% and Δ_v = 0.3%.

Parameter	Value	Parameter	Value
Inductor	86.6 µH	Load resistance	15.64 Ω
Output capacitor	18.4 µF	Duty cycle	0.345
Switching frequency	100 kHz	Input current ripple	3% = 4.017 A
Input Voltage	201.6 V	Output voltage	0.3% =1.95 V
Output Voltage	650 V	Peak Power	27 kW

Wolfspeed's C3M0032120K model is preferred for the SiC-MOSFET. The model is the 3rd generation technology product of the series. It was chosen because of its features, such as high switching speed with low capacitances and high blocking voltage with low on-resistance. As a result of these characteristics, switching losses can be minimized, system efficiency can be improved, and power density can be raised. For the SiC diode, STMicroelectronics' STPSC40H12CWL model is preferred. This model has a 1200 V-rated and features a low forward voltage drop (V_F) architecture. Schottky structure prevents the appearance of reverse recovery loss during the turn-off phase. The dual structure provides high power integration for the reduced PCB form factor. The parameters of preferred SiC-based semiconductors are shown in Table 5.5.

Table 5.5. Properties of SiC-based semiconductors.

Semiconductor Type	SiC-MOSFET	Semiconductor Type	SiC Schottky Diode
Manufacturer	Wolfspeed	Manufacturer	STMicroelectronics
Model	C3M0032120K	Model	STPSC40H12CWL
V_{DS}	1200 V	V_{RRM}	1200 V
I_D	63 A	$I_{F(AV)}$	2*20 A
$Rds_{(on)}$	32 mΩ	$V_{F\ (Typ)}$	1.35 V
$T_{j\ (max.)}$	175 °C	$T_{j\ (max.)}$	175 °C

V_{DS} = Drain to Source Voltage, I_D= Continuous Drain Current, $Rds_{(on)}$= Drain to Source On-State Resistance.

Figure 5.14. shows the circuit of the SiC-based MDIBC at 100 kHz with Δ_i= 3% and Δ_v = 0.3%. In that circuit , Q_1, Q_2, Q_3, and Q_4 are SiC-type MOSFETs, V_{DC} is the DC power supply, V_{P1}, V_{P2}, V_{P3}, and V_{P4} are pulse voltages , R_1, R_2, R_3, R_4 gate resistors D_1, D_2, D_3, and D_4 are body diodes of SiC-type MOSFETs, D_5, D_6, D_7, and D_8 are SiC Schottky diodes, L_1 and L_2 are

inductors, C_o is the output capacitor, C_1, C_2, C_3, C_4 are shunt capacitors, and R_L is the load resistor of the circuit. For the simulation of C3M0032120K and STPSC40H12CWL semiconductors, simulation models provided by Wolfspeed [52] and STMicroelectronics [53] were used in PSpice software, respectively.

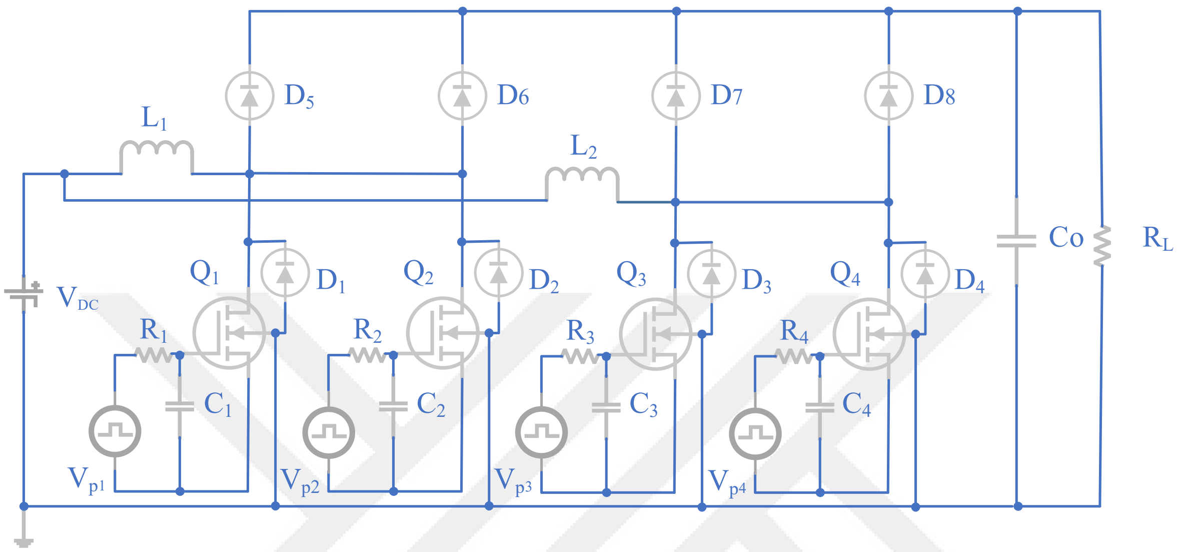

Figure 5.14. PSpice simulation circuit of the SiC-based MDIBC at 100 kHz with Δ_i= 3% and Δ_v = 0.3%.

Figure 5.15 shows the voltage and current ripple waveforms of SiC-based MDIBC running in PSpice software. According to the simulation results, it's seen that the waveform of the output voltage ripple varies between 650.528 V and 648.477 V, which is an acceptable range and satisfies the voltage ripple requirement in Table 5.4. Besides, the current ripple of the converter is consistent with the calculated value which is meeting the current ripple requirement.

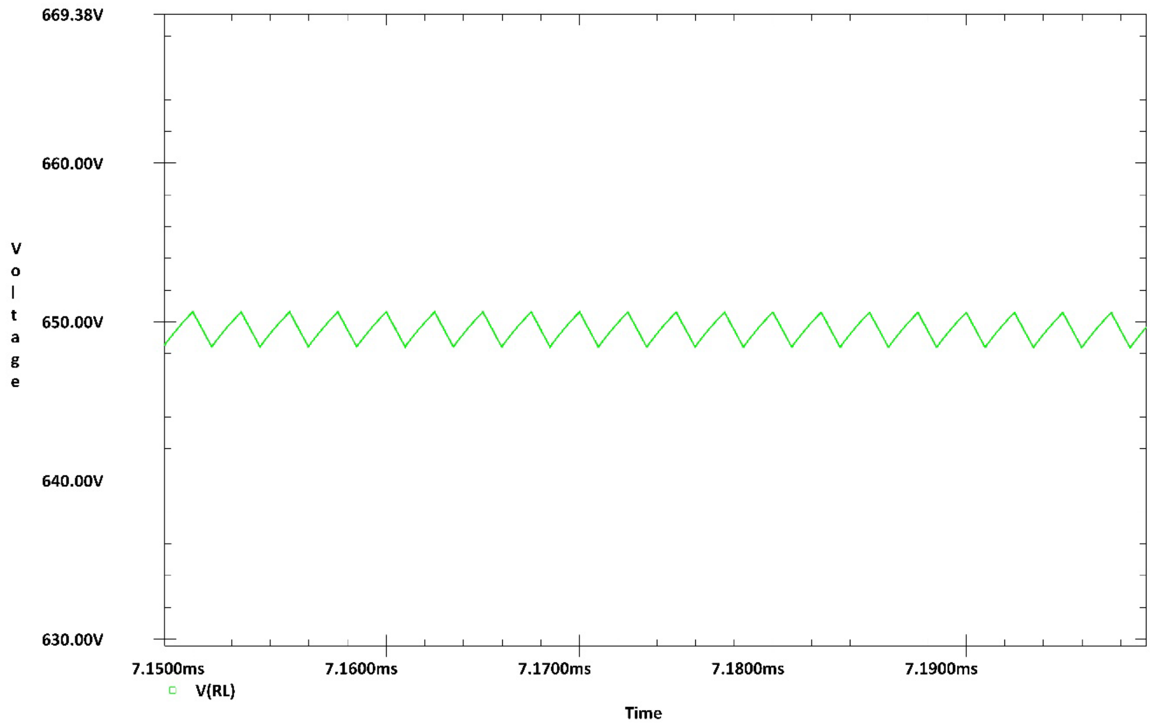

(a)

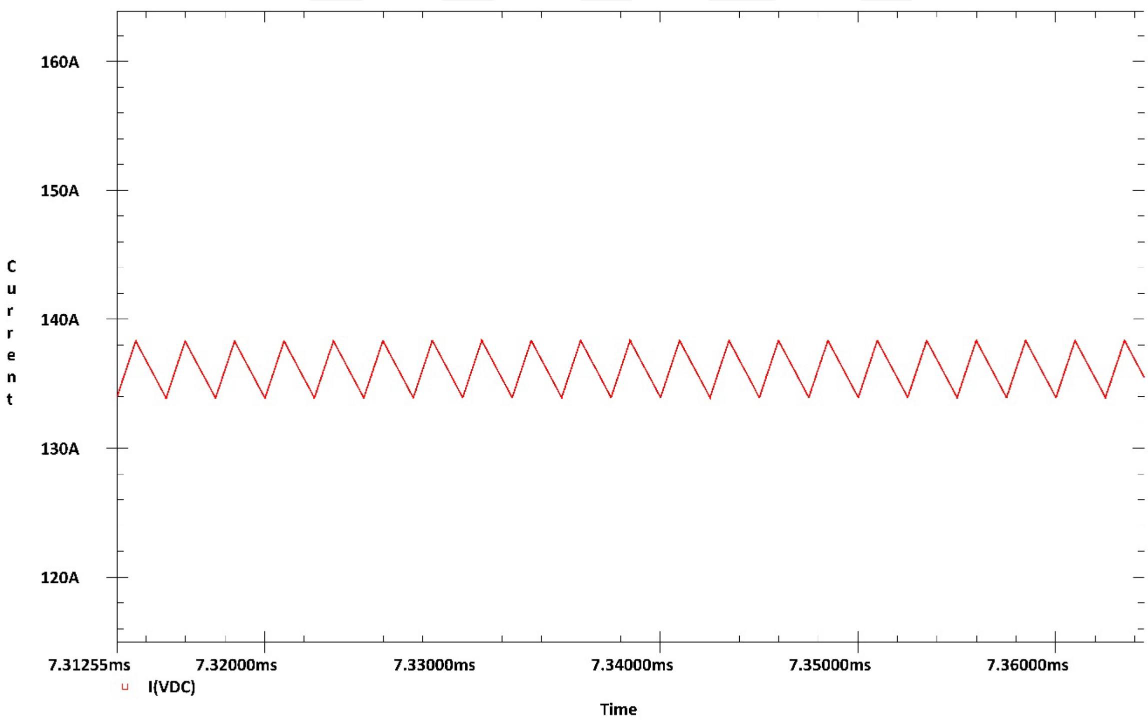

(b)

Figure 5.15. (a) Output voltage ripple, (b) Input current ripple.

Figure 5.16. shows the inductor current waveform. Having a 180° phase shift between inductors results in twice as much ripple current at the same frequency.

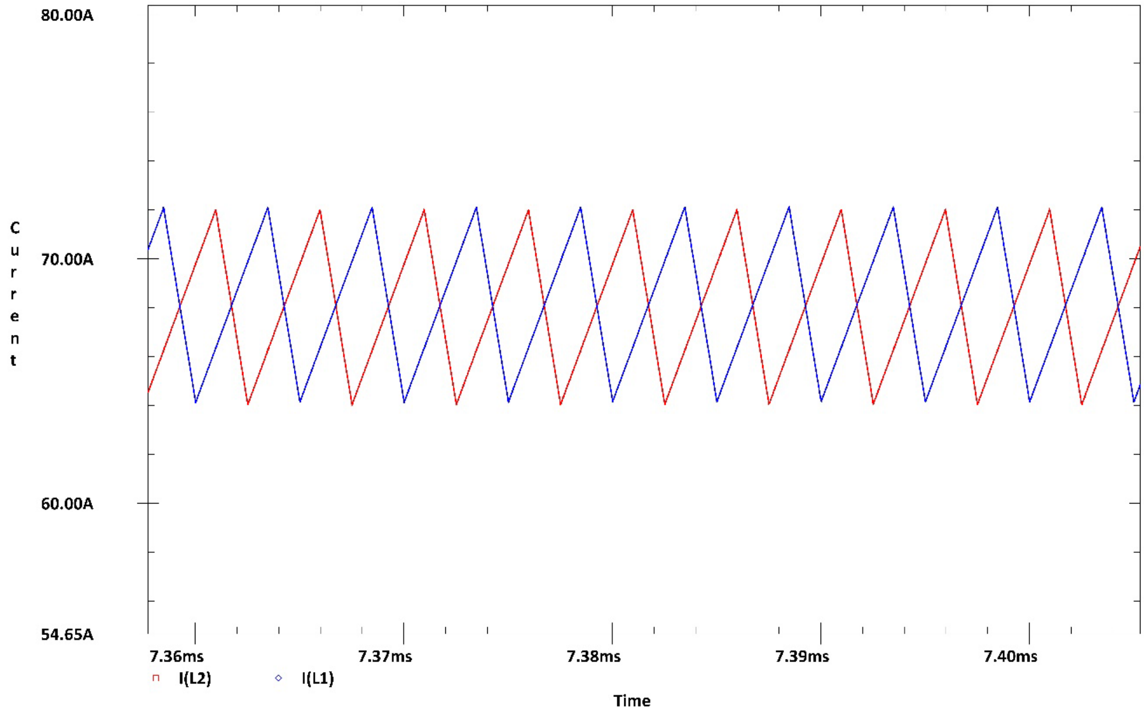

Figure 5.16. Inductor current waveform.

SiC-MOSFET conduction power loss is determined using Equations 5.6 and 5.7.

$$I_{ds(rms)} = I_{ds(on)}\sqrt{D} \tag{5.6}$$

$$P_{cond\_loss} = I_{ds(rms)}^2 R_{ds_{(on)}} \tag{5.7}$$

Where $I_{ds(rms)}$ is the root mean square (RMS) value of drain to source current at ON state. Notably, the $I_{ds(on)}$ value is derived from the current wave graph of a SiC MOSFET as shown in Figure 5.17. According to the current waveform, $I_{ds(rms)}$ value is calculated as 39.84 A.

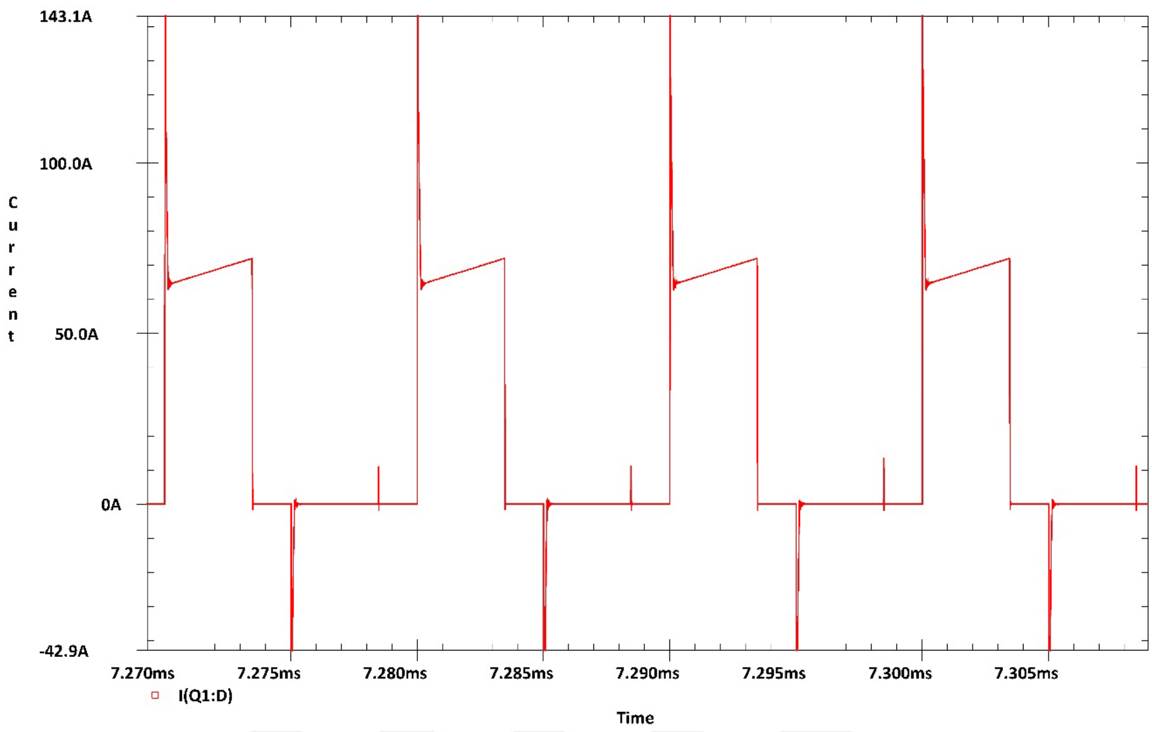

Figure 5.17. The current waveform of SiC-MOSFET.

To determine the $R_{ds_{(on)}}$ value, the graphs provided in the C3M0032120K datasheet and shown in Figure 5.18. is used. According to graphs, $R_{ds_{(on)}}$ value is determined as approximately 46.2 mΩ. The derived values result in a conduction loss of 73.72 W for each SiC-MOSFET. Since there are four SiC-MOSFETs in the converter, so total conduction loss of the converter is 293.28 W.

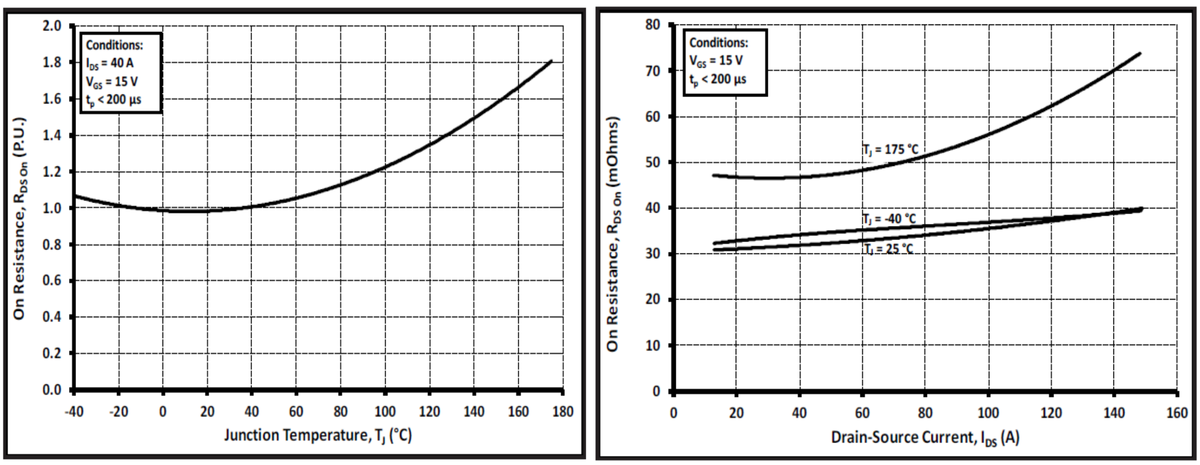

Figure 5.18. $R_{ds_{(on)}}$ value, according the junction temperature 125 °C and drain-source current [52].

SiC-MOSFET semiconductor switching power loss is determined with the use of the aforementioned Equation 5.2. In order to calculate the E_{ON} and E_{OFF} values, 3 graphs in the C3M0032120K datasheet were used and shown in Figure 5.19. The values were calculated according to 650 V and 125 °C conditions. Since the values in the graphs are determined according to 600 V and 800 V output voltages and 25 °C and 125 °C temperature conditions and the SiC-based MDIBC has 650 V output voltage, in order to obtain a more accurate result, the E_{ON} and E_{OFF} values are calculated according to the values at 600 volts and 800 volts firstly. Then, the equivalent of 650 V output voltage was determined at 125 °C conditions.

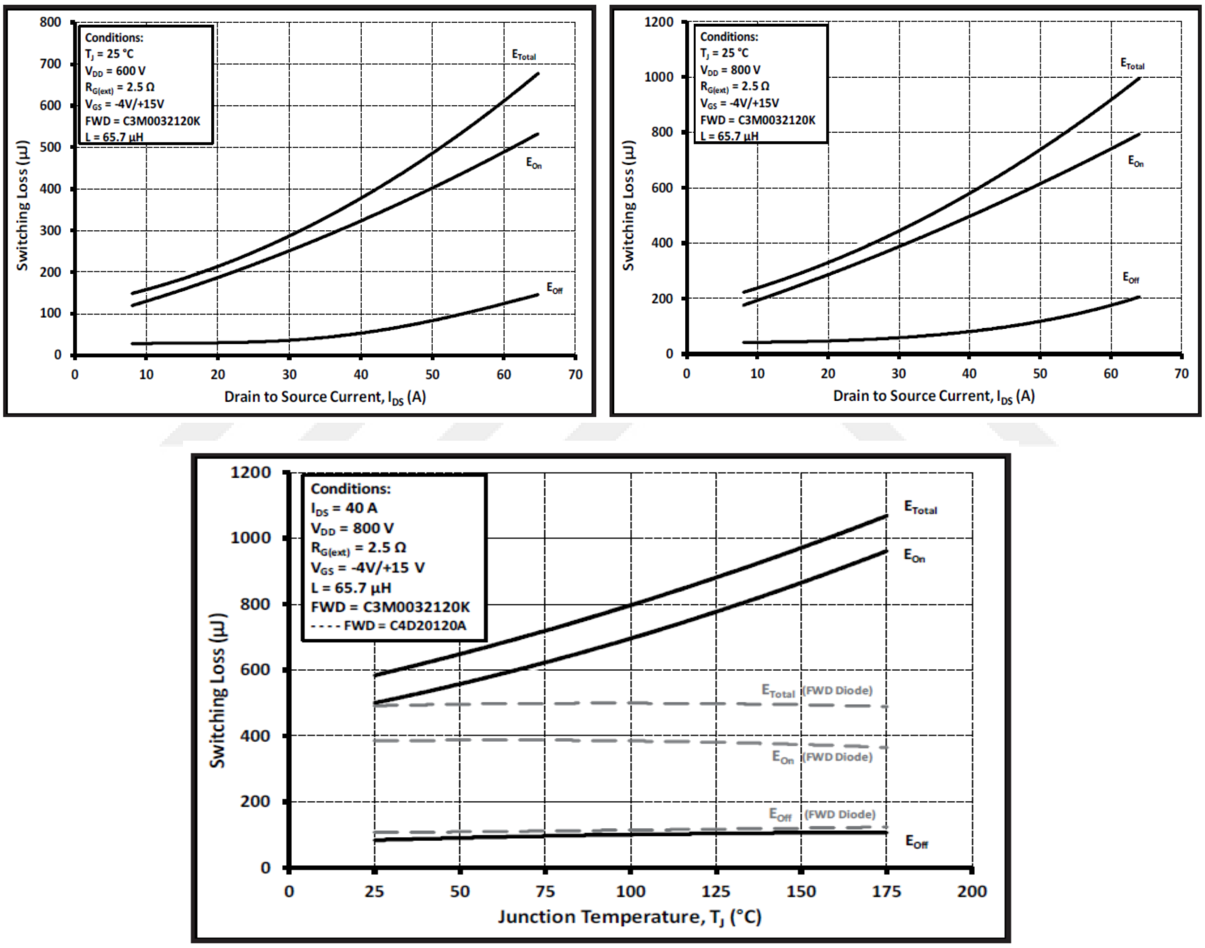

Figure 5.19. The top left figure is switching loss to drain to source current graph at 600 V at 25 °C. The top right figure is switching loss to drain to source current graph at 800 V at 25 °C. The bottom figure is the switching loss to the junction temperature graph at different temperature conditions [52].

According to graphs the E_{ON} and E_{OFF} values were calculated as approximately 1170 µJ in total. Since the switching frequency is 100 kHz, the switching loss of the SiC-MOSFET is 117 W. With four SiC-MOSFETs, the switching losses add up to 468 W.

Using Equation 5.8, we can determine the power lost in conduction by the SiC diode. Due to the absence of reverse recovery current, the switching loss of SiC Schottky diodes is zero.

$$P_{dcondloss} = V_F I_{(avr)} \tag{5.8}$$

$I_{(avr)}$ value is derived from the current waveform of the SiC Schottky diode in Figure 5.20.

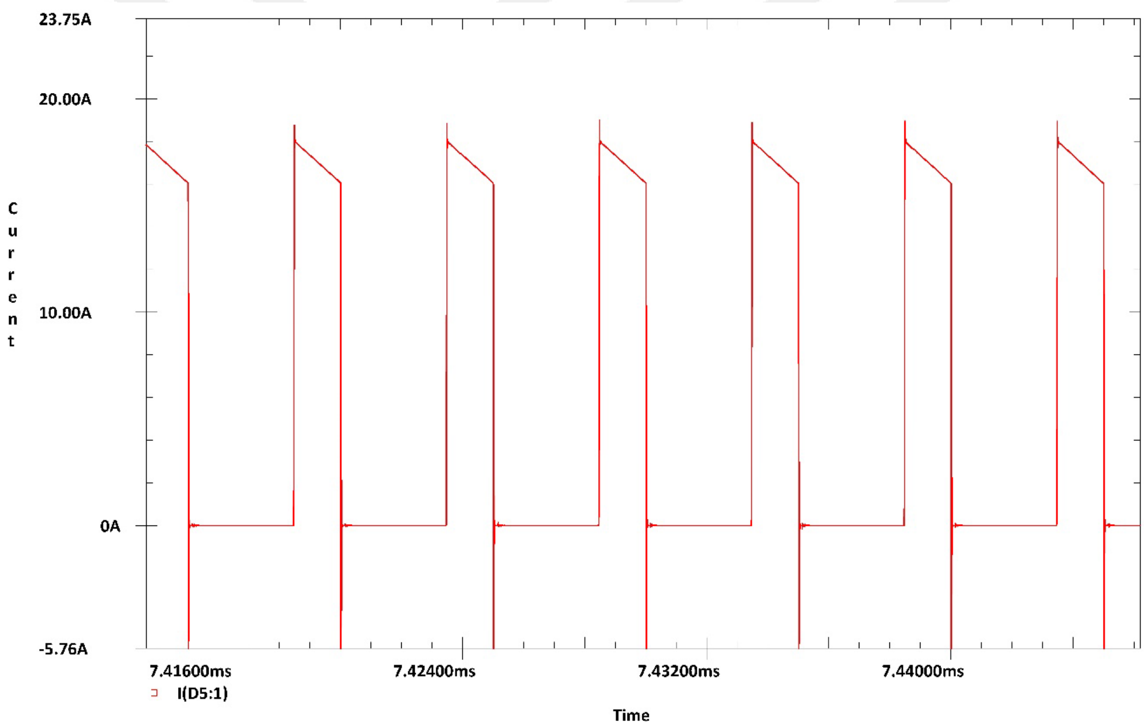

Figure 5.20. The current waveform of SiC Schottky diode.

According to the graph, the average diode current value is obtained as 5.27 A. For the determination of the V_F value, the forward voltage drop versus forward current curves in the datasheet of STPSC40H12C was used and shown in Figure 5.21.

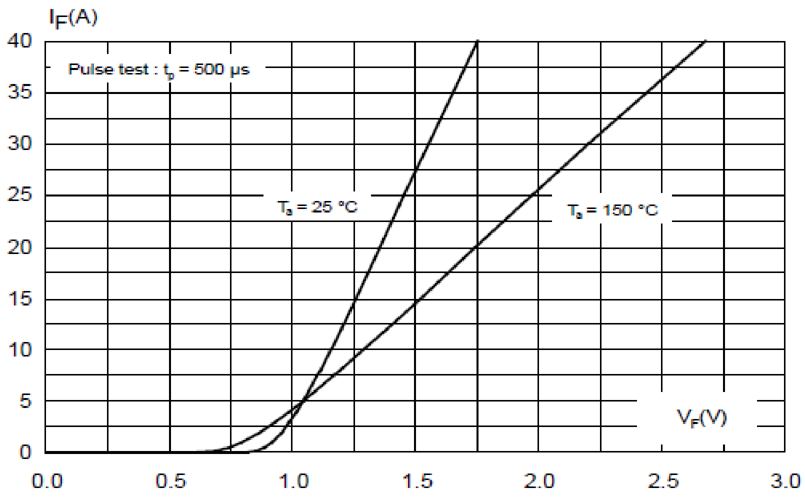

Figure 5.21. Forward voltage drop versus forward current curves of STPSC40H12C per diode [53].

From the graph above we can see that the V_F value is approximately 1.5 V per diode at 125 °C. Each SiC diode, which has a dual structure, has a conduction loss of 15.81 W. There are four SiC diode devices in the converter, so the total SiC diode conduction loss of the converter is 63.24 W.

Table 5.6. shows the inductor design parameters and losses.

Table 5.6. Inductor design parameters and losses.

Parameters	Inductance
Manufacturer	Micrometals
Part Number	T650-2
Stack	1
Shape	Toroid
Inductance Value	86,6 µH
Frequency	100 kHz
Core Loss	5.29 W
Conductor Loss	16.48 W
Total Loss	21.77 W

Table 5.6's information reveals that the converter's total inductor loss is calculated to be 43.54 W due to the presence of two inductors. The total conduction loss of the converter is 293.28 W. The converter's overall switching loss is 468 W. Total SiC diode loss of the converter is 63.24 W. It's apparent from obtained values, the total power loss of the SiC-based MDIBC is 868.06 W. According to this total power loss, the converter efficiency is calculated as 96.78%.

Using the power loss calculation equations at the 100 kHz switching frequency of SiC-based MIDBC, the total power losses, efficiency, and corresponding inductor and capacitor values at 80 kHz, 60 kHz, and 40 kHz switching frequencies are calculated and shown in Table 5.7. Table 5.8. shows the converter parameters previously mentioned as the second stage and calculated when the Δ_i= 10%, Δ_v = 0.3%.

Table 5.7. The parameter values correspond to different frequencies of the SiC-based MDIBC at Δ_i= 3% and Δ_v = 0.3%.

SiC-BASED MDIBC				Δ_i= 3%, 4.017 A Δ_v = 0.3%, 1.95V
Frequency	**Total Power Loss(W)**	**Efficiency (%)**	**Inductor Value (µH)**	**Capacitor Value (µF)**
100 kHz	868.06	96.78	86.6	18.4
80 kHz	778.33	97.11	108.2	23
60 kHz	695.82	97.42	144.28	30.6
40 kHz	635.17	97.64	216.4	46

Table 5.8. The parameter values correspond to different frequencies of the SiC-based MDIBC at Δ_i= 10% and Δ_v = 0.3%.

SiC-BASED MDIBC				Δ_i= 10%, 13.392 A Δ_v = 0.3%, 1.95V
Frequency	**Total Power Loss(W)**	**Efficiency (%)**	**Inductor Value (µH)**	**Capacitor Value (µF)**
100 kHz	852.74	96.84	26	18.4
80 kHz	756.14	97.20	33	23
60 kHz	663.49	97.54	44	30.6
40 kHz	593.7	97.8	65	46

Calculated values from Table 5.8 can be compared with the calculated values in Table 5.7, it is seen that the dimensions of the inductor have decreased further and the efficiency of the converter has increased. Figure 5.22 shows the power loss chart, efficiency chart, and inductor chart of SiC-based MDIBCs with respect to Si-IGBT-based Toyota Prius.

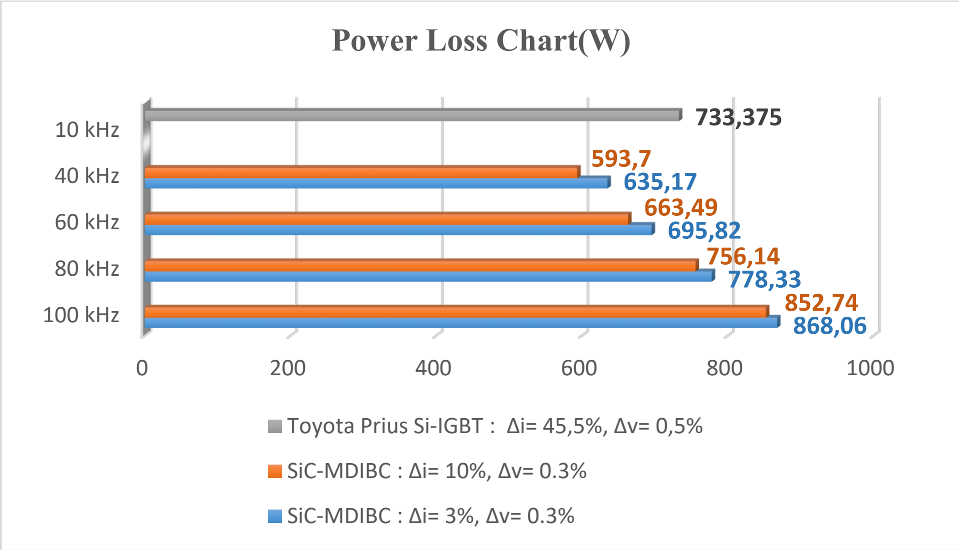
Power Loss Chart(W)
10 kHz
40 kHz
60 kHz
80 kHz
100 kHz
733,375
593,7
635,17
663,49
695,82
756,14
778,33
852,74
868,06
0
200
400
600
800
1000
Toyota Prius Si-IGBT : Δi= 45,5%, Δv= 0,5%
SiC-MDIBC : Δi= 10%, Δv= 0.3%
SiC-MDIBC : Δi= 3%, Δv= 0.3%

(a)

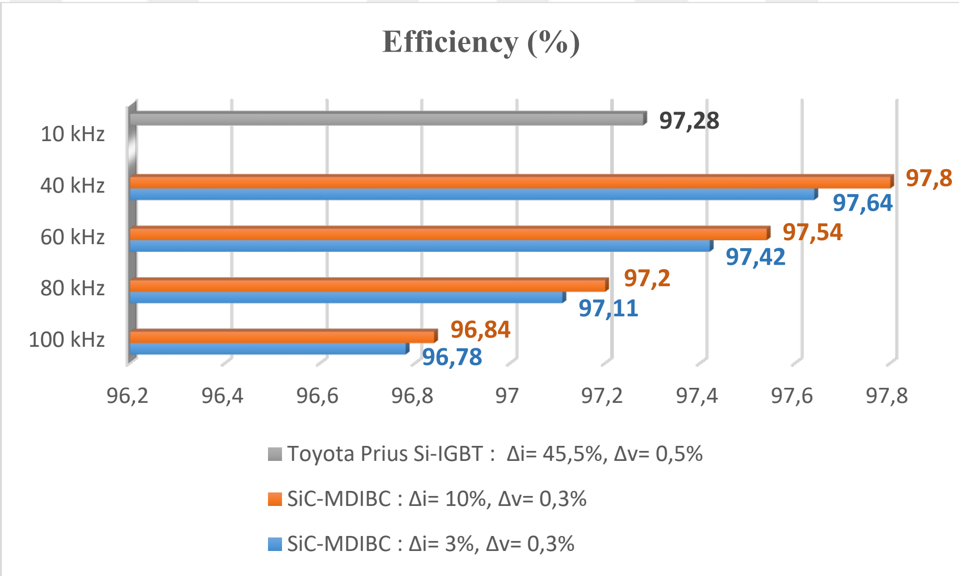
Efficiency (%)
10 kHz
40 kHz
60 kHz
80 kHz
100 kHz
97,28
97,8
97,64
97,54
97,42
97,2
97,11
96,84
96,78
96,2
96,4
96,6
96,8
97
97,2
97,4
97,6
97,8
Toyota Prius Si-IGBT : Δi= 45,5%, Δv= 0,5%
SiC-MDIBC : Δi= 10%, Δv= 0,3%
SiC-MDIBC : Δi= 3%, Δv= 0,3%

(b)

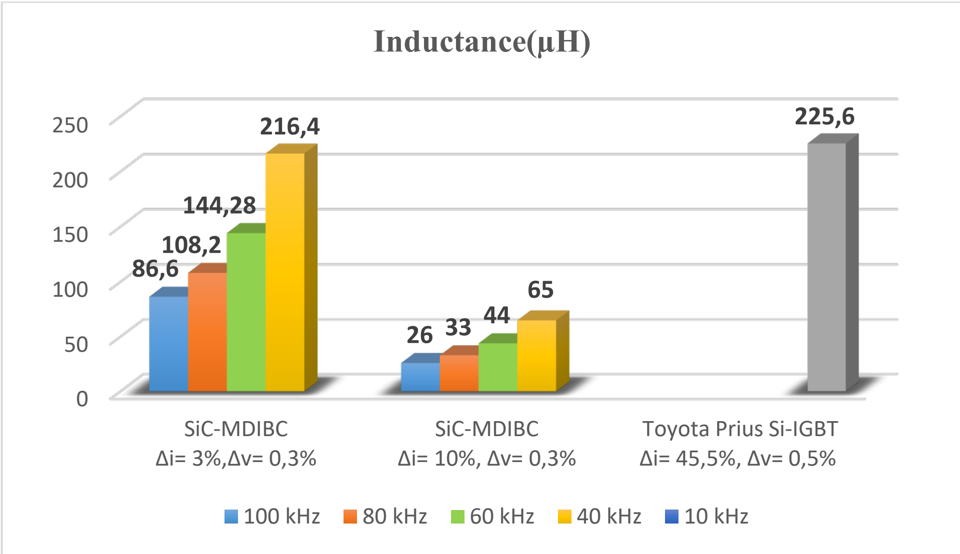

(c)

Figure 5.22. Comparative results of SiC-based MDIBC at Δ_i= 3% and Δ_v = 0.3%, SiC-based MDIBC at Δ_i= 10% and Δ_v = 0.3%, and Si-IGBT-based Toyota Prius in terms of (a) power loss, (b) efficiency and (c) inductance size.

5.3. Analysis of GaN-based MDIBC

GaN-based MDIBC was analyzed in two stages as was SiC-based MDIBC. To compare GaN-based MDIBC with SiC-based MDIBC and Si-IGBT-based Prius, input voltage, output voltage, and converter power must be the same. Design parameters of GaN-based MDIBC were calculated using Equations 4.22., 4.23., 4.24., and 4.25. and Table 5.9. shows the GaN-based MDIBC topology at 100 kHz designed according to the first stage (Δ_i= 3% and Δ_v = 0.3%).

Table 5.9. GaN-based MDIBC parameters at 100 kHz with Δ_i= 3% and Δ_v = 0.3%.

Parameter	Value	Parameter	Value
Inductor	86.6 µH	Load resistance	15.64 Ω
Output capacitor	18.4 µF	Duty cycle	0.345
Switching frequency	100 kHz	Input current ripple	3% = 4.017 A
Input Voltage	201.6 V	Output voltage ripple	0.3% =1.95 V
Output Voltage	650 V	Peak Power	27 kW

The model GS-065-060-5-T-A which is an automotive-grade 650 V enhancement mode GaN power transistor was preferred design of the GaN-based MDIBC. The high switching frequency (>10 MHz), zero reverse recovery loss, a small PCB footprint (9 x 7.6 mm2), and reverse conduction capabilities are just some of the benefits of this transistor. This model is designed to be cooled using a heat sink on the top of the device that offers very low junction-to-case thermal resistance for demanding high-power applications. Besides, it has a 900 V drain-to-source voltage pulse to insure a blocking voltage margin. Since the devices will be exposed to voltage stress equal to the output voltage (650 V) during operation, this margin will be good for the reliability of the converter [54]. Just as DC/DC converter efficiency is mainly determined by switching frequency losses, GaN transistors outperform SiC transistors in terms of efficiency and power density thanks to their lower parasitic capacitances and gate charges [55, 56]. GaN transistors also have very small turn-on (T_{ON}) and turn-off (T_{OFF}) switching times than SiC semiconductors, this feature also contributes to their lower switching power losses [57]. Table 5.10. shows the comparative parameters of GS-065-060-5-T-A model GaN transistor and C3M0032120K model SiC MOSFET.

Table 5.10. Parameters comparison between GS-065-060-5-T-A [54] and C3M0032120K [52] models.

Manufacturer		**GaN Systems GS-065-060-5-T-A**	**Wolfspeed C3M0032120K**
Parameter	**Symbol**	**Value**	**Value**
Drain to Source Voltage	V_{DS}	650 V	1200 V
Continuous Drain Current	I_D	60 A	63 A
Drain to Source On-State Resistance	$R_{DS(on)}$	25 mΩ	32 mΩ
Total Gate Charge	$Q_{G(tot)}$	14 nC	118 nC
Reverse Recovery Charge	Q_{RR}	0	478 nC
Input Capacitance	C_{ISS}	516 pF	3357 pF
Output Capacitance	C_{OSS}	127 pF	129 pF
Gate to Source Threshold	$V_{GS(th)}$	1.1-2.6 V	1.8-3.6 V

As with SiC-based MDIBC, STMicroelectronics' STPSC40H12CWL model SiC diode was preferred for the design of GaN-based MDIBC. The parameters of preferred GaN transistor and SiC Schottky diode are shown in Table 5.11.

Table 5.11. Properties of GaN transistor and SiC Schottky diode.

Semiconductor Type	GaN Transistor	Semiconductor Type	SiC Schottky Diode
Manufacturer	GaN Systems	Manufacturer	STMicroelectronics
Model	GS-065-060-5-T-A	Model	STPSC40H12CWL
V_{DS}	650 V	V_{RRM}	1200 V
I_D	60 A	$I_{F(AV)}$	2*20 A
$Rds_{(on)}$	25 mΩ	$V_{F\ (Typ)}$	1.35 V
$T_{j\ (max.)}$	150 °C	$T_{j\ (max.)}$	175 °C

Figure 5.23. shows the circuit of the a non-isolated unidirectional GaN-based MDIBC structure. In this structure, V_{DS} represents the direct current power source, while V_{P1}, V_{P2}, V_{P3}, and V_{P4} represent the pulse voltages. Q_1, Q_2, Q_3, and Q_4 are all GaN transistors; L_1, L_2 are inductors, D_1, D_2, D_3 and D_4 are all SiC Schottky diodes; C_1 is the output capacitor; R_1, R_2, R_3, R_4 and R_L are gate and load resistors respectively. For the simulation of GS-065-060-5-T-A and STPSC40H12CWL semiconductors, simulation models provided by GaN Systems [54] and STMicroelectronics [53] were used in PSpice software accordingly.

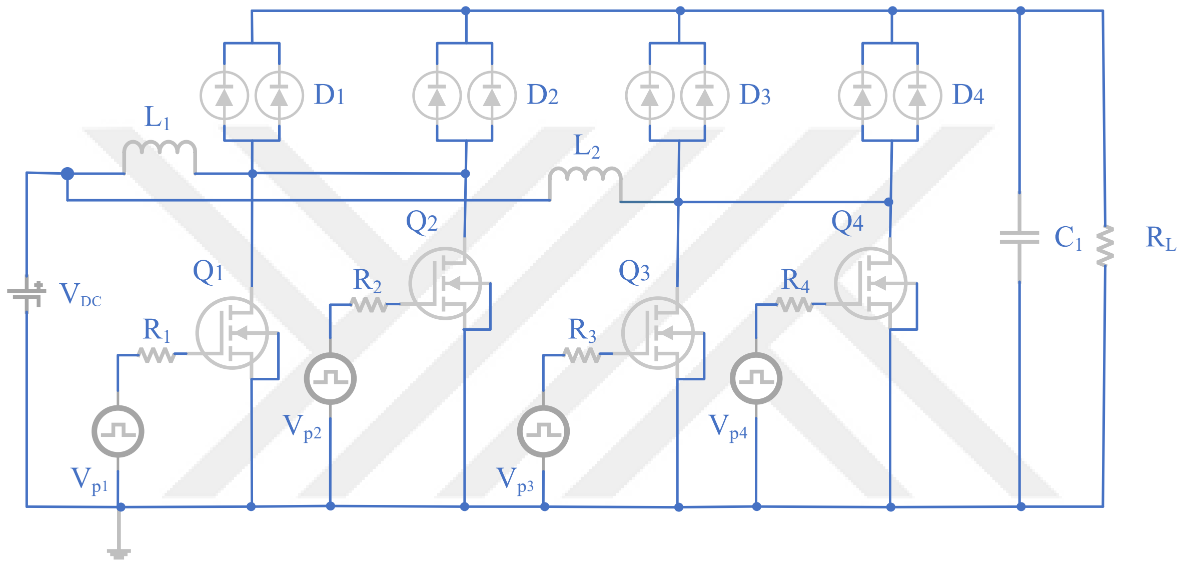

Figure 5.23. The circuit of the non-isolated unidirectional GaN-based MDIBC structure.

GaN-based MDIBC is evaluated at the same design parameters as SiC-based MDIBC, therefore their current and voltage ripple waveforms, as well as their inductor current ripple waveforms, as depicted in Figure 5.24 are relatively similar.

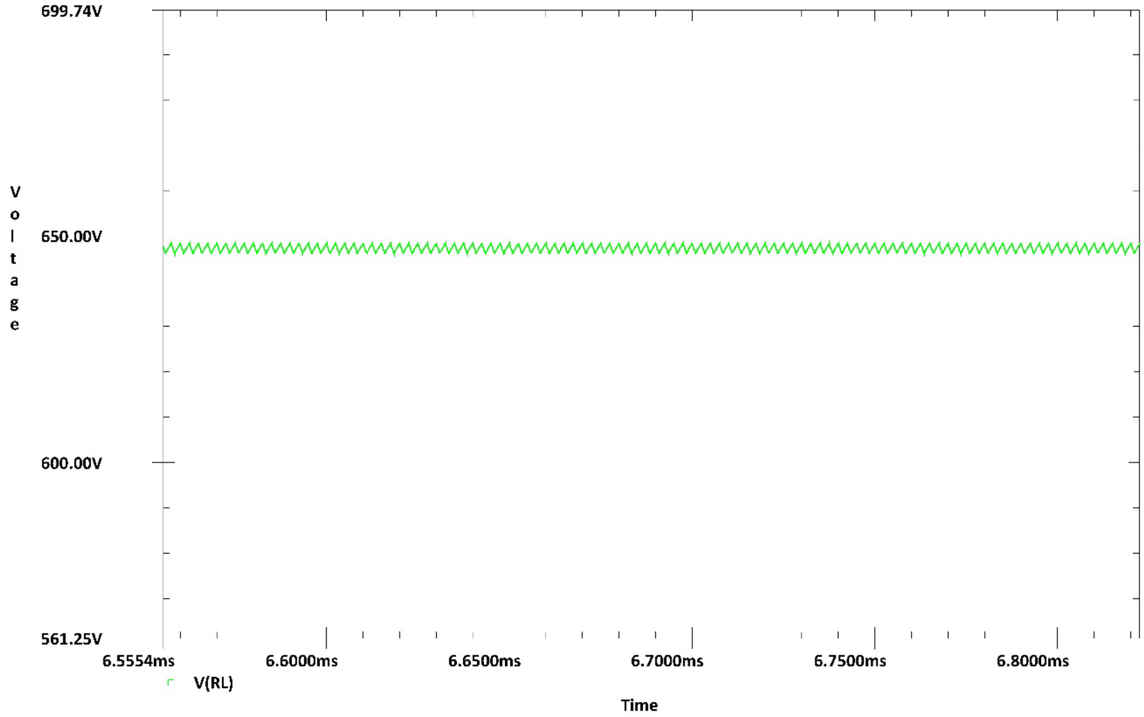
699.74V
650.00V
600.00V
561.25V
Voltage
6.5554ms
6.6000ms
6.6500ms
6.7000ms
6.7500ms
6.8000ms
V(RL)
Time

(a)

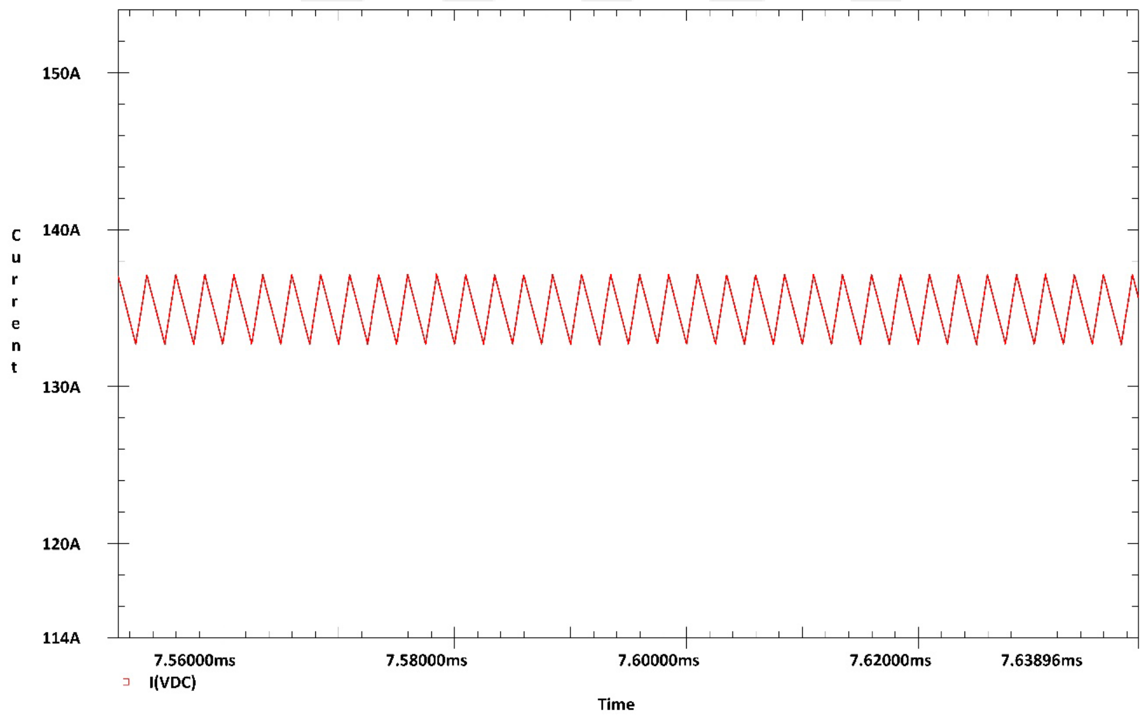
150A
140A
130A
120A
114A
Current
7.56000ms
7.58000ms
7.60000ms
7.62000ms
7.63896ms
I(VDC)
Time

(b)

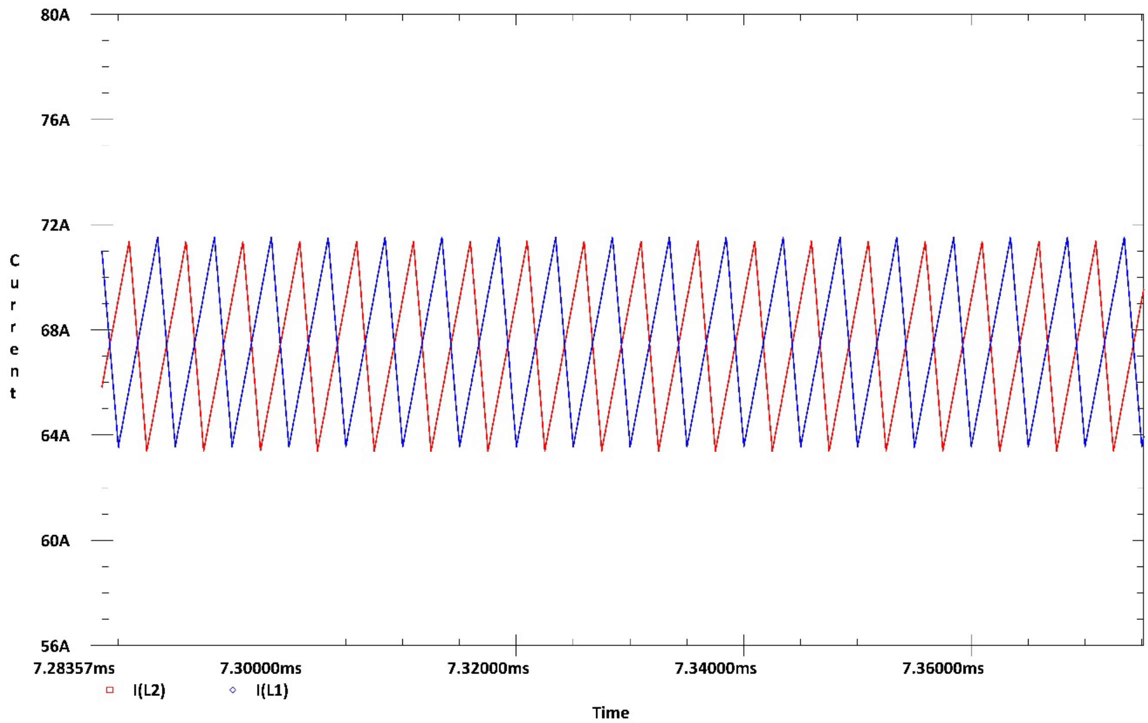

(c)

Figure 5.24. (a) Output voltage ripple, (b) Input current ripple, (c) Inductor current ripple waveforms of GaN-based MDIBC.

Equations 5.9 and 5.10 are used to determine the GaN transistor's conduction power loss.

$$I_{ds(rms)} = I_{ds(on)}\sqrt{D} \tag{5.9}$$

$$P_{cond\_loss} = I^2_{ds(rms)} R_{ds_{(on)}} \tag{5.10}$$

Figure 5.25. shows the current waveform of the GaN transistor. $I_{ds(on)}$ value is obtained according to the current waveform, and then $I_{ds(rms)}$ value is calculated as 39.64 A.

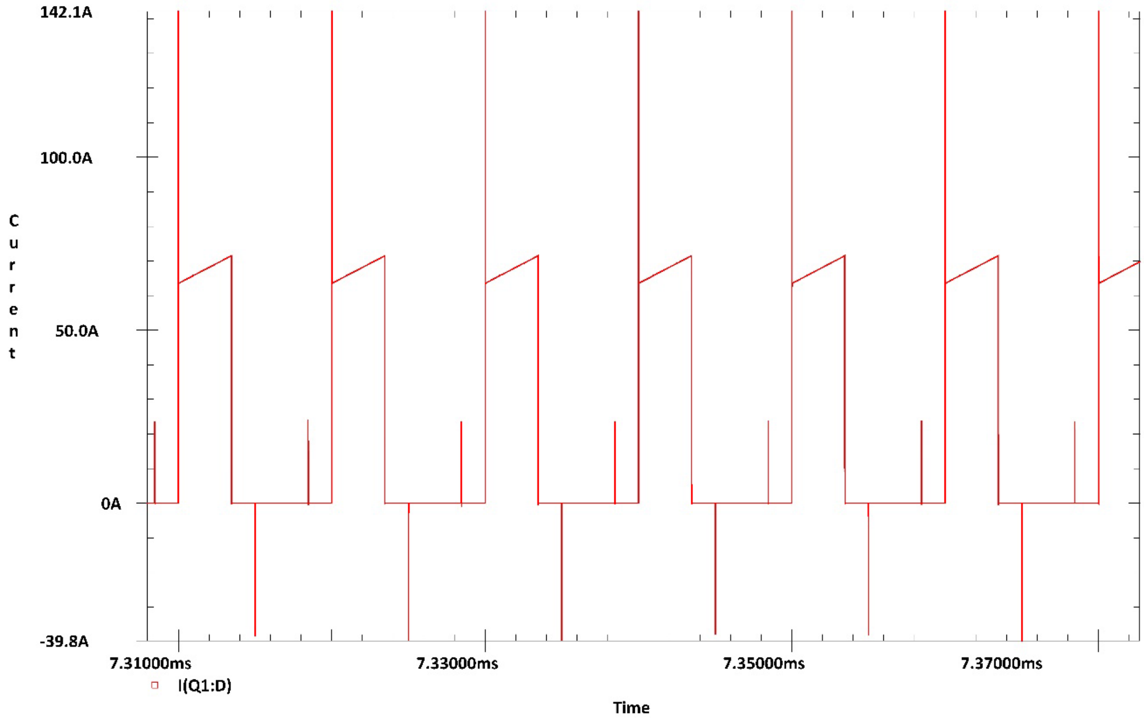

Figure 5.25. The current waveform of the GaN transistor.

The $R_{ds_{(on)}}$ value was obtained from the datasheet of GS-065-060-5-T-A. Figure 5.26 shows the $R_{ds_{(on)}}$ to I_{ds} characteristics curves [54]. According to these curves, the $R_{ds_{(on)}}$value was calculated as approximately 58.25 mΩ at 125 °C.

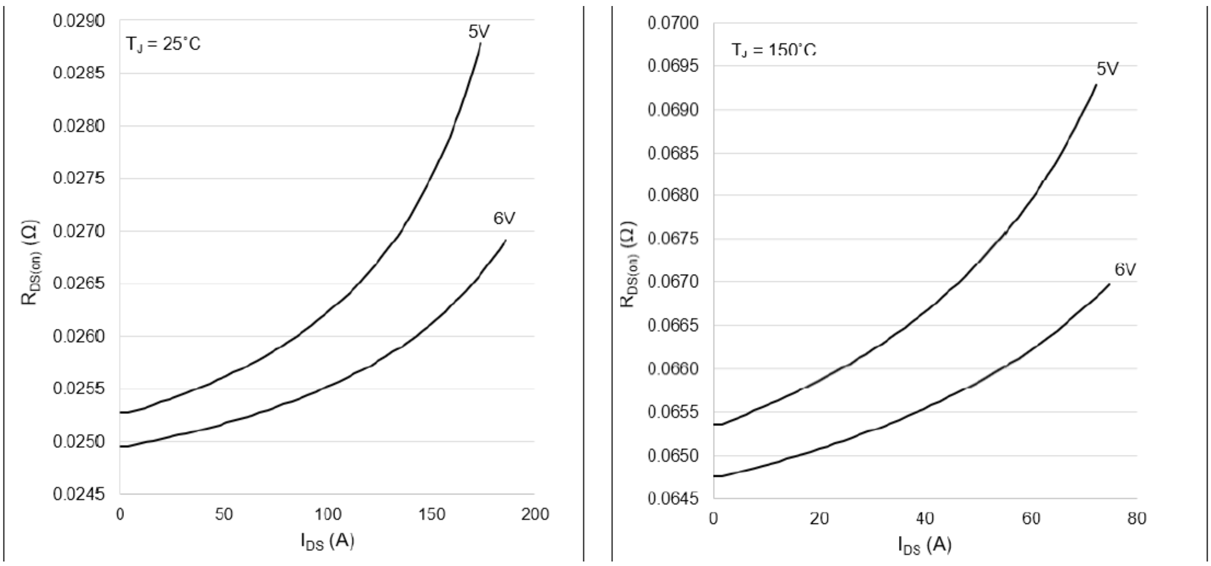

Figure 5.26. The $R_{ds_{(on)}}$ to I_{ds} characteristics curves. The left side curve is at 25 °C and the right side curve is at 150 °C.

According to obtained values, the conduction power loss of each GaN transistor is 91.53 W. Since there are four GaN transistors in the converter, the total conduction power loss of the converter is 366.12 W.

Equation 5.11 is used to determine the GaN transistor's switching power loss.

$$P_{sw\_loss} = V_{DS} I_D f_{sw} \frac{T_{ON} + T_{OFF}}{2} \tag{5.11}$$

Where T_{ON} is the switching time during the ON transition, T_{OFF} is the switching time during the OFF transition.

In Figure 5.27, the voltage waveform of the GaN transistor and the T_{ON} and T_{OFF} switching time transitions are shown individually.

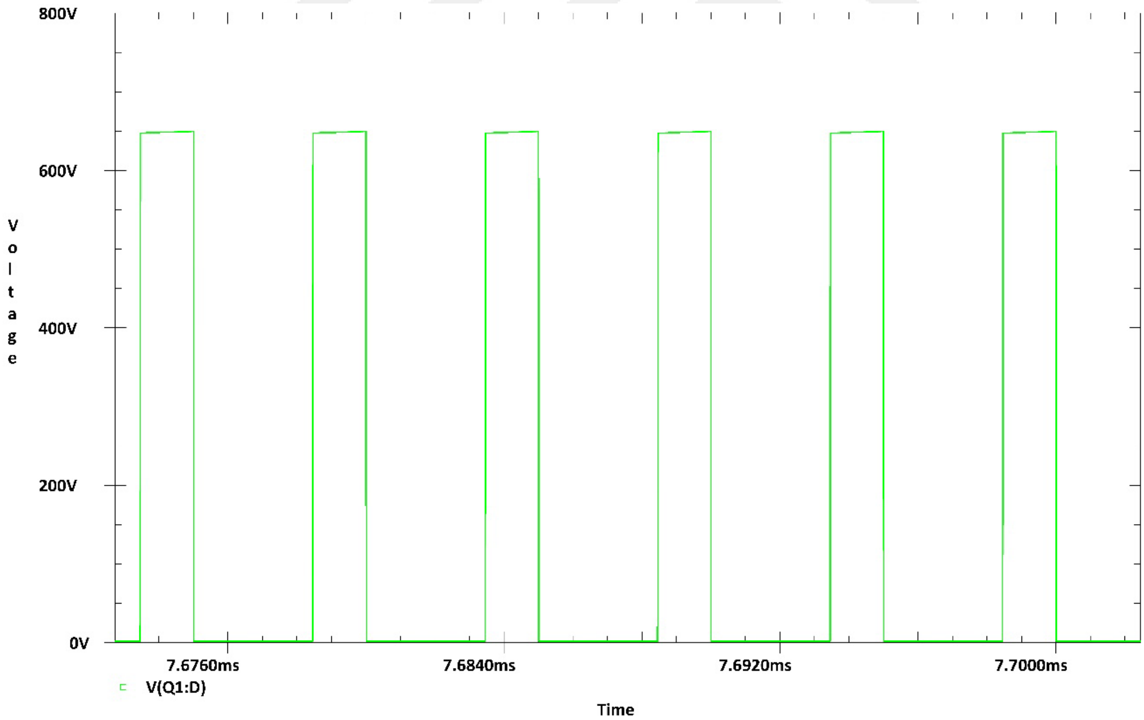

(a)

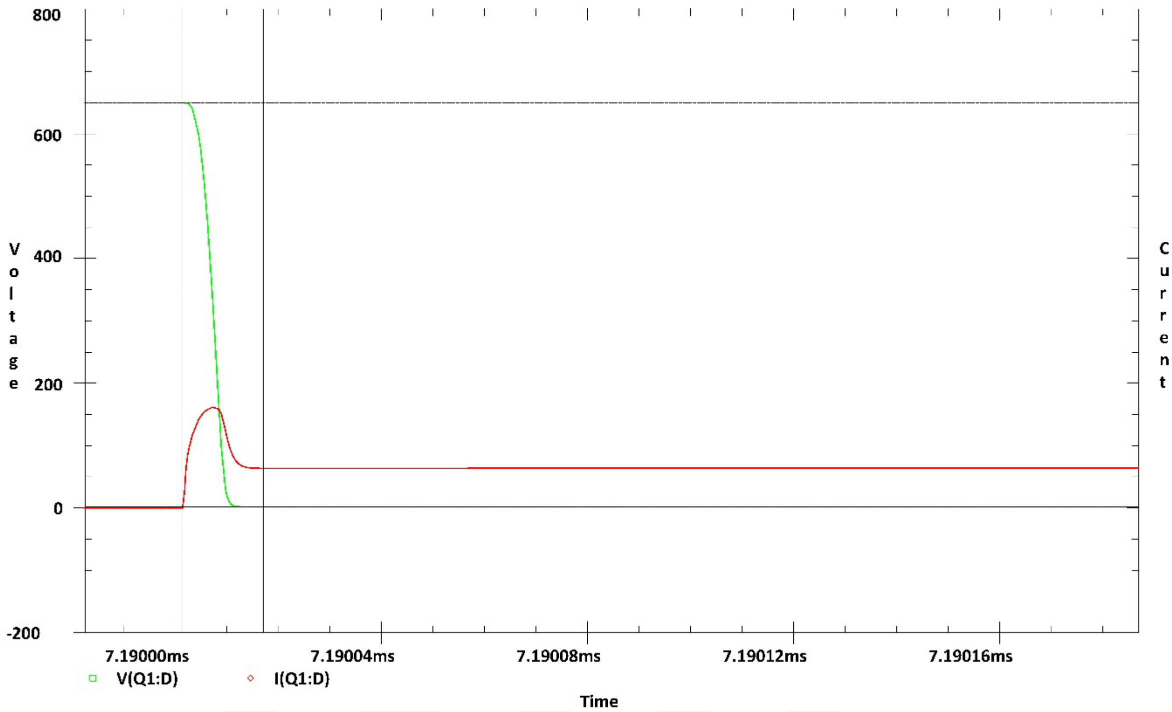

(b)

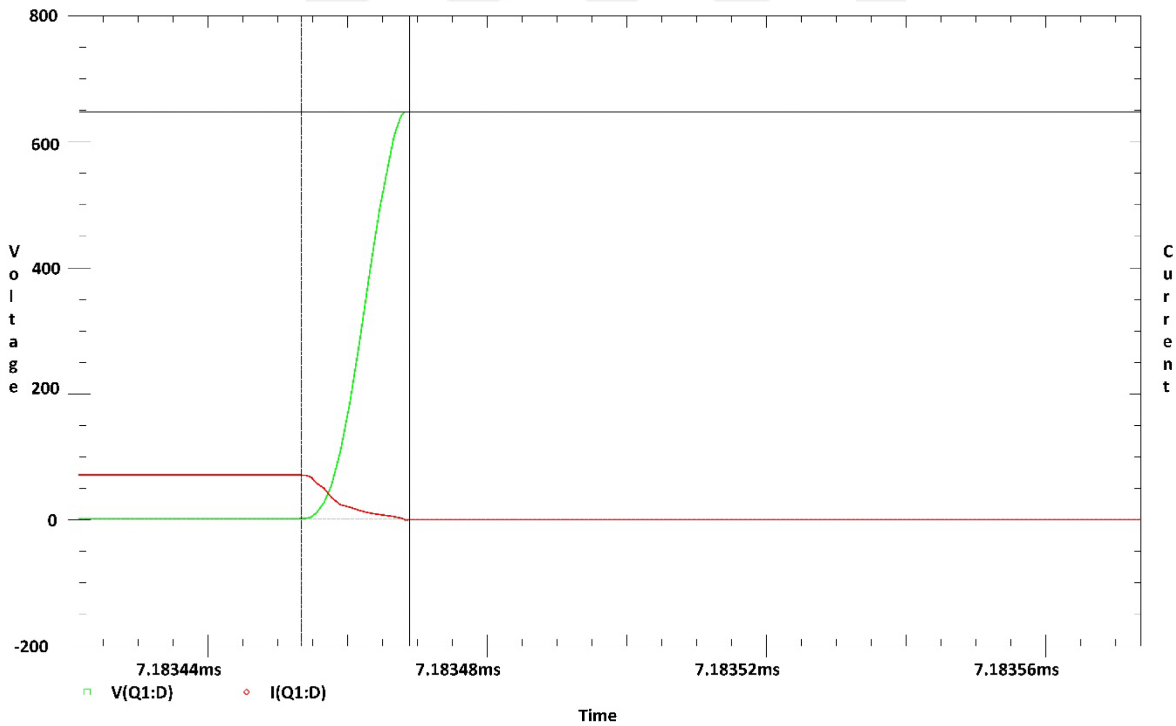

(c)

Figure 5.27. (a) The voltage waveform of the GaN transistor, (b) The T_{ON} switching time transition, (c) The T_{OFF} switching time transition.

According to the values obtained from Figures 5.25 and 5.27, the switching power loss of the GaN transistor at 100 kHz is calculated as 61.28 W. As there are four GaN transistors in the converter, the total switching power loss of the converter is 245.12 W.

Since the SiC Schottky diode has a dual structure and consists of two diodes per device, according to the current waveform of the SiC Schottky diode as shown in Figure 5.28, the average current per diode is calculated as 5.23 A. The forward voltage drop is calculated approximately as 1.5 V at 125 °C shown before in Figure 5.21. Using Equation 5.8., the total SiC Schottky diode conduction loss is calculated as 62.76 W.

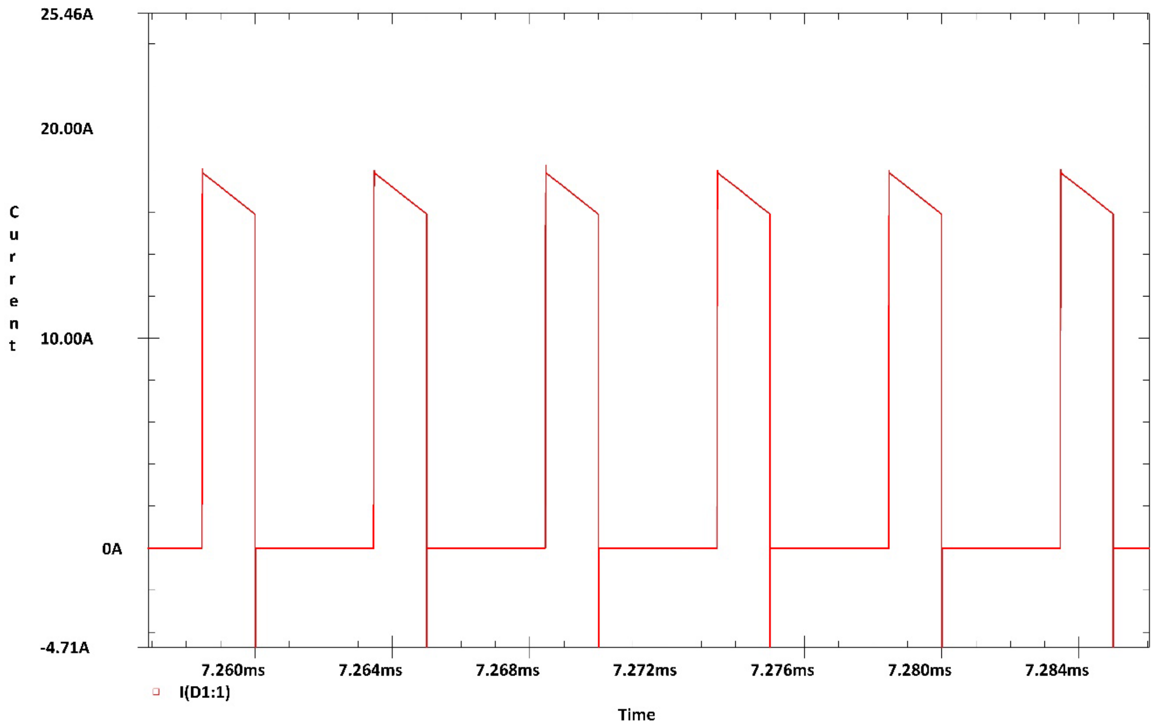

Figure 5.28. The current waveform of SiC Schottky diode.

Due to GaN-based MDIBC being designed using the same parameters as SiC-based MDIBC at 100 kHz with Δ_i= 3% and Δ_v = 0.3%, the total inductor power loss is equal to each other. Therefore total inductor loss of the GaN-based MDIBC is 43.54 W.

Equation 5.12 shows the reverse recovery loss of the GaN transistor. Based on Table 5.10., the Q_{RR} value is zero for the GaN transistor. Therefore this power loss has no effect on the calculation.

$$P_{rrl} = V_{DS} f_{sw} Q_{RR} \tag{5.12}$$

Equation 5.13 shows the gate loss of the GaN transistor where V_{GS} and $Q_{G(tot)}$, the gate to source voltage, and total gate charge of the corresponding device subsequently. Since the $Q_{G(tot)}$ value is very small and almost has no effect on the calculation, this power loss was not taken into account in this study.

$$P_{gate\_loss} = V_{DS} f_{sw} Q_{G(tot)} \tag{5.13}$$

According to calculated values, the total conduction loss of the converter is 366.12 W. The total switching loss of the converter is 245.12 W. Total SiC diode loss of the converter is 62.76 W. The total inductor loss of the GaN-based MDIBC is 43.54 W. When we calculate the above-mentioned power losses, the total power loss of the GaN-based MDIBC is 717.54 W. According to this total power loss, the efficiency of the converter was calculated as 97.34%.

Using the power loss calculation equations at the 100 kHz switching frequency of GaN-based MIDBC, the total power losses, efficiency, and corresponding inductor and capacitor values at 80 kHz, 60 kHz, and 40 kHz switching frequencies are calculated and shown in Table 5.12. Table 5.13. shows the converter parameters previously mentioned as the second stage and calculated when the Δ_i= 10%, Δ_v = 0.3%.

Table 5.12. The parameter values correspond to different frequencies of the GaN-based MDIBC at Δ_i= 3% and Δ_v = 0.3%.

GaN-BASED MDIBC				Δ_i= 3%, 4.017 A Δ_v = 0.3%, 1.95V
Frequency	**Total Power Loss(W)**	**Efficiency (%)**	**Inductor Value (µH)**	**Capacitor Value (µF)**
100 kHz	717.54	97.34	86.6	18.4
80 kHz	687.52	97.45	108.2	23
60 kHz	652.14	97.58	144.28	30.6
40 kHz	626.31	97.68	216.4	46

Table 5.13. The parameter values correspond to different frequencies of the GaN-based MDIBC at Δ_i= 10% and Δ_v = 0.3%.

GaN-BASED MDIBC				Δ_i= 10%, 13.392 A Δ_v = 0.3%, 1.95V
Frequency	**Total Power Loss(W)**	**Efficiency (%)**	**Inductor Value (µH)**	**Capacitor Value (µF)**
100 kHz	724.24	97.31	26	18.4
80 kHz	683.24	97.47	33	23
60 kHz	621.55	97.69	44	30.6
40 kHz	584.19	97.83	65	46

From the data in Table 5.12. and 5.13, we can see that the efficiency values of the GaN-based MDIBC are greater than the Si-IGBT-based Toyota Prius' converter(97.28%), even at 100 kHz. As mentioned before while the switching frequency decreases, the inductor and the capacitor sizes increase. When the ripple factor is an important criterion for the design of the converter, Table 5.12. shows that GaN-based MDIBC reached the highest efficiency value at 40 kHz with 216.4 (µH) and 46 (µF) inductor and capacitor values correspondingly. These passive component values are also lower than the Toyota Prius' (225 µH, 888 µF). Considering this ripple factor, the input current ripple was reduced by 93.4% and the output voltage ripple by 40% with GaN-based MDIBC.

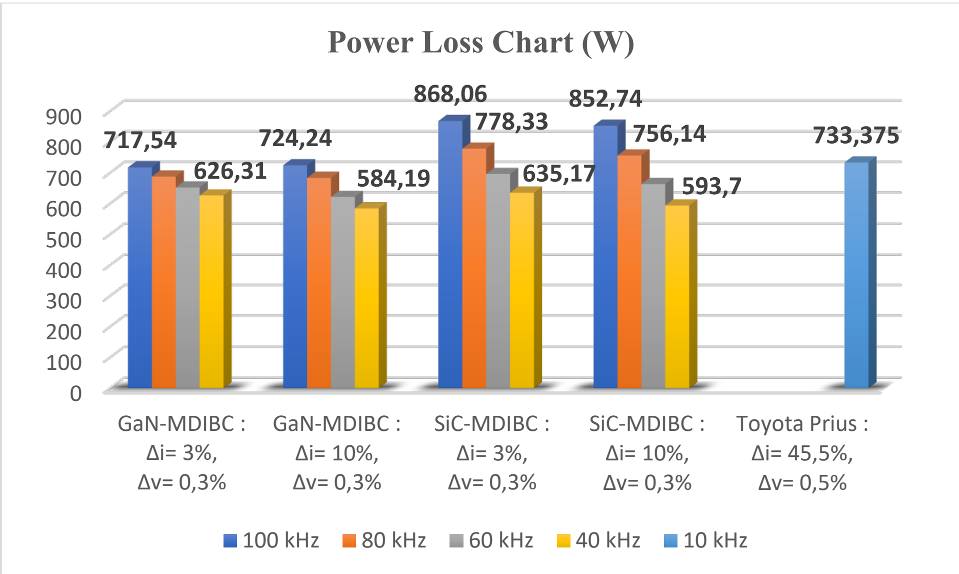

(a)

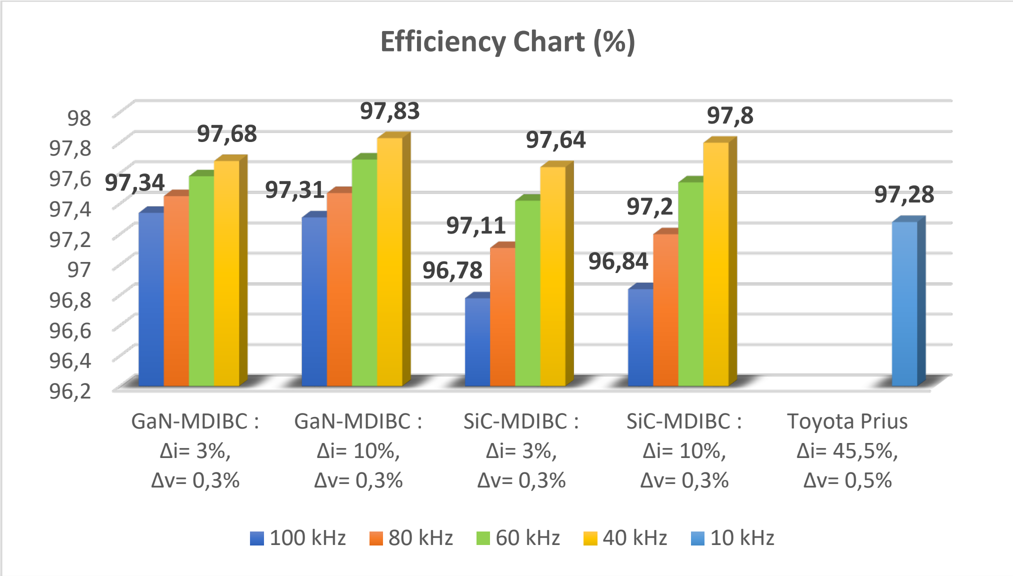

(b)

Figure 5.29. (a) The power loss chart, (b) The efficiency chart of the GaN-based MDIBC, the SiC-based MDIBC, and the Si-IGBT-based Prius at different switching frequencies.

According to the calculated values in Figure 5.29., it's obvious that while the power losses of SiC-based MDIBC at 100 kHz and 80 kHz are higher than Prius, lower power loss is obtained with GaN-based MDIBC even at 100 kHz. With these power losses, the SiC-based MDIBC's efficiencies at 100 kHz and 80 kHz are lower than the Prius. The highest efficiency value of 97.83% is reached with GaN-based MDIBC at 40 kHz when Δ_i= 10% and Δ_v = 0.3%. Another point to be noted is that all the efficiency values of GaN-based MDIBC are higher than Prius. These results indicate that GaN semiconductor has low power losses even at high frequencies.

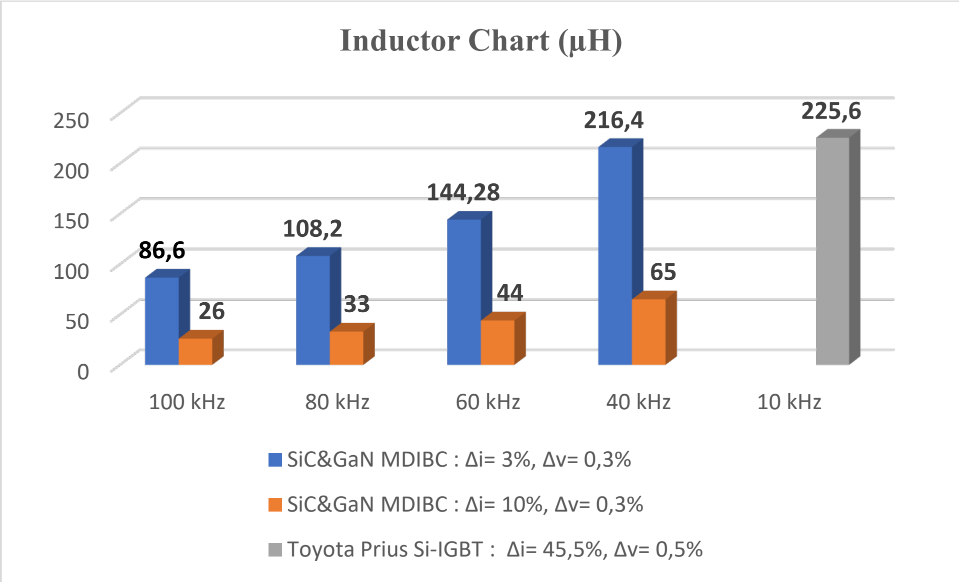

(a)

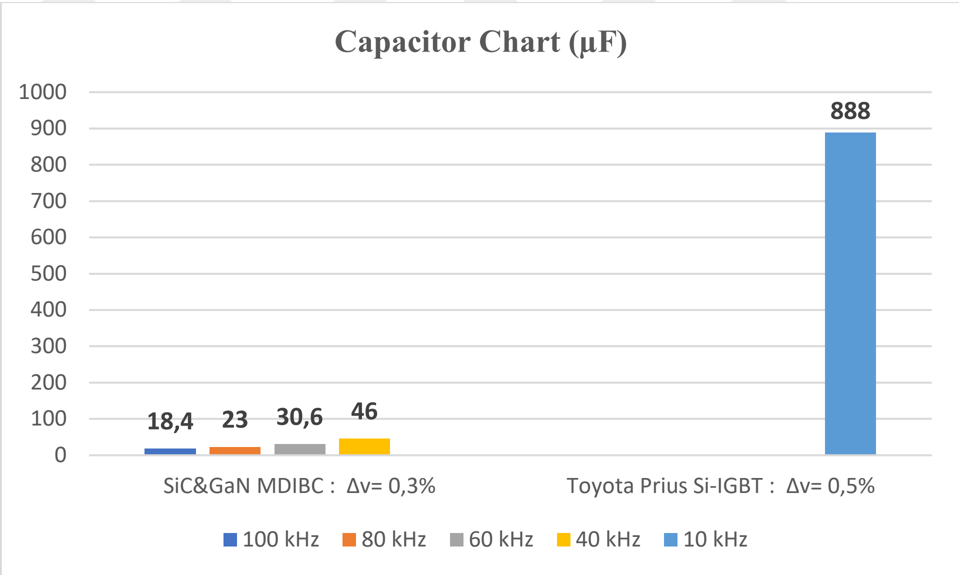

(b)

Figure 5.30. Passive component charts (a) Inductance, (b) Capacitor.

Figure 5.30 shows the variation of inductor and capacitor values used in converters depending on frequency. It can be seen in Figure 5.30, the inductor and capacitor sizes decrease as the switching frequency increases. Since power density is an important criterion in EVs, decreasing the size of the inductor and capacitor contributes to the increase in power density. With GaN-based MDIBC, the inductor value is reduced by approximately 88.5% at 100 kHz switching frequency compared to the Toyota Prius' converter. In addition, the capacitor value was decreased from 888 µF to 18.4 µF, resulting in a decrease of 97.92%. With these reductions, the power density of the vehicle was increased with GaN-based MDIBC, and the volume and weight of the passive components were decreased. Considering the contribution of weight reduction to the fuel economy of the vehicle, it is obvious that it will contribute to the vehicle's being more preferred in the commercial market.

6. CONCLUSION

In this study, the 2010 Toyota Prius 27 kW Si-IGBT-based converter was redesigned with SiC-based MDIBC and GaN-based MDIBC. The designed SiC-based MDIBC and GaN-based MDIBC were simulated in PSpice (17.4) software. These three converter structures were compared in terms of efficiency, power loss, inductor and capacitor size, and input current ripple and output voltage ripple. The MDIBC was chosen for its success in reducing inductor and capacitor size, as well as its success in reducing current and voltage ripples.

Comparisons were performed in two stages. In the first stage, current and voltage ripple levels were kept quite low. For this purpose, 3% input current ripple and 0.3% output voltage ripple values were determined not to surpass the inductor and capacitor values of the benchmark converter for switching frequencies of 100 kHz, 80 kHz, 60 kHz, and 40 kHz. SiC-based MDIBC and GaN-based MDIBC were designed at these switching frequencies and specified ripple conditions. In the simulation results, at 3% input current ripple and 0.3% output voltage ripple conditions, SiC-based MDIBC performed lower efficiency than the benchmark converter at 100 kHz and 80 kHz switching frequency, whereas its efficiency was greater than the benchmark converter at 60 kHz and 40 kHz switching frequency. On the other hand, with GaN-based MDIBC, higher efficiency was achieved than the benchmark converter at all four mentioned switching frequency values.

In the second stage to improve power density and efficiency, the inductor size was reduced while the input current ripple was raised to 10%. SiC-based MDIBC and GaN-based MDIBC were simulated at the above-mentioned switching frequencies and 10% input current ripple and 0.3% output voltage ripple conditions. In the simulation results, 97.8% efficiency was obtained with SiC-based MDIBC and 97.83% efficiency with GaN-based MDIBC at 40 kHz. The SiC-based MDIBC resulted in lower efficiency than the benchmark converter at 80 kHz and 100 kHz switching frequencies. Again with GaN-based MDIBC, higher efficiency was obtained at all four switching frequencies than the benchmark converter. When the switching frequencies dropped below 60 kHz, there was a little difference in efficiency between SiC-based MDIBC and GaN-based MDIBC. GaN-based MDIBC performed better at switching frequencies of 80 kHz and above.

With GaN-based MDIBC, the inductor value was reduced by 88.5% and the capacitor value by 97.92% at 100 kHz switching frequency without falling below the efficiency value of the Toyota Prius Si-IGBT-based converter. Thus, with the smaller inductor and capacitor value, the weight of the converter was reduced, the power density was increased, and fuel savings were achieved, considering the positive effect of the weight reduction on the fuel economy.

It is proven that GaN semiconductor is less affected by switching losses than SiC semiconductor, even at high frequencies. Although switching losses increase at high frequencies, due to the fact that GaN semiconductor is less affected by these losses, inductor and capacitor sizes can be reduced further, and efficiency can still be kept high by designing converters at higher frequencies in future studies.

While the cost of SiC and GaN semiconductors is still higher than the Si semiconductor and the high number of components in the MDIBC topology increases costs, it is obvious that these costs will be compensated in a short time considering the high efficiency achieved with the SiC and GaN-based MDIBC topology, the reduction in the size of passive components and the decrease in costs, as well as the contribution of the weight reduction of passive components to fuel economy in EVs.

REFERENCES

[1] S. Chakraborty, H.-N. Vu, M. Hasan, D. Tran, M. El Baghdadi, and O. Hegazy, "DC-DC Converter Topologies for Electric Vehicles, Plug-in Hybrid Electric Vehicles and Fast Charging Stations: State of the Art and Future Trends," *Energies,* vol. 12, p. 1569, 04/25 2019, doi: 10.3390/en12081569.

[2] A. Sivaprasad, J. Joseph, S. Kumaravel, and S. Ashok, "Design and analysis of a dual input DC-DC converter for hybrid electric vehicle," in *2015 IEEE International Conference on Signal Processing, Informatics, Communication and Energy Systems (SPICES)*, 19-21 Feb. 2015, pp. 1-5, doi: 10.1109/SPICES.2015.7091466.

[3] S. G. Dil, "DAHA ÇEVRECİ BİR ULAŞIM SEKTÖRÜ İÇİN ELEKTRİKLİ ARAÇLAR ÇÖZÜM MÜ?," *Antalya Ticaret ve Sanayi Odası Vizyon,* 2021,October 22. [Online]. Available: https://www.atsovizyon.org.tr/daha-cevreci-bir-ulasim-sektoru-icin-elektrikli-araclar-cozum-mu/.

[4] D. Navamani, L. Anbazhagan, and V. Krishnasamy, "Implementation of voltage controlled Multi Device Interleaved Boost Converter using FPGA," *International Review on Modelling and Simulations,* 06/30 2014, vol. 7, pp. 422-427, doi: 10.15866/iremos.v7i3.1238.

[5] "Electric Vehicle Myths," *United States Environmental Protection Agency(EPA),* 2022, October 18. [Online]. Available: https://www.epa.gov/greenvehicles/electric-vehicle-myths.

[6] "How much emissions do electric cars produce?," *Usa Facts,* 2022, September 1. [Online]. Available: https://usafacts.org/articles/how-much-emissions-do-electric-cars-produce/.

[7] "Emissions from Electric Vehicles," *U.S. Department of Energy*. [Online]. Available: https://afdc.energy.gov/vehicles/electric_emissions.html.

[8] H. Zorlu, "İlk Elektrikli Otomobil Aslında Neden, Ne Zaman ve Nasıl Üretildi?," *WebTekno,* 2022. [Online]. Available: https://www.webtekno.com/ilk-elektrikli-otomobil-ne-zaman-ve-nasil-uretildi-h116773.html.

[9] K. A. WILSON, "Worth the Watt: A Brief History of the Electric Car, 1830 to Present," *Car and Driver,* 2022, August 17. [Online]. Available: https://www.caranddriver.com/features/g15378765/worth-the-watt-a-brief-history-of-the-electric-car-1830-to-present/.

[10] S. Kocabey, "Elektrikli Otomobillerin Dünü, Bugunü ve Geleceği," Conference Paper February 28 2018. [Online]. Available: https://dergipark.org.tr/tr/pub/jitsa/issue/35759/396912.

[11] R. MATULKA, "The History of the Electric Car," *Energy.gov,* 2014, September 15. [Online]. Available: https://www.energy.gov/articles/history-electric-car.

[12] "TOGG: Yerli Otomobil TOGG Ne Zaman Çıkacak, Özellikleri, Fiyatı," *Otonakit*. [Online]. Available: https://www.otonakit.com/blog-detay/togg-yerli-otomobil-togg-ne-zaman-cikacak-ozellikleri-fiyati#:~:text=TOGG%20yerli%20otomobil%2C%20T%C3%BCrkiye'nin,5%20model%20modelle%20piyasaya%20%C3%A7%C4%B1kacak.

[13] O. Şen, "Performance Evaluation of SiC-Based Multidevice Interleaved Boost Converter for Electric Vehicles," M.S.thesis, Dept. Electronics Information and Bioengineering, Politechnico di Milano University, Milan, Italy, 2020.

[14] O. Hegazy, J. V. Mierlo, and P. Lataire, "Analysis, Modeling, and Implementation of a Multidevice Interleaved DC/DC Converter for Fuel Cell Hybrid Electric Vehicles,"

IEEE Transactions on Power Electronics, vol. 27, no. 11, pp. 4445-4458, 2012, doi: 10.1109/TPEL.2012.2183148.
[15] M. S. Priya and R. Balasubramanian, "Analysis of multidevice interleaved boost converter for high power applications," in *2014 International Conference on Circuits, Power and Computing Technologies [ICCPCT-2014]*, 20-21 March 2014, pp. 320-327, doi: 10.1109/ICCPCT.2014.7054946.
[16] N. H. Abu Khanipah, M. Azri, Z. Ibrahim, and N. Abd Rahim, "Multi device interleaved DC/DC converter for fuel cell applications," vol. 8, pp. 41-45, 01/01 2016.
[17] S. Ramalingam, "Design, Simulation and Hardware Implementation of a Multi Device Interleaved Boost Converter for Fuel Cell Applications," *International Journal of Power Electronics and Drive Systems (IJPEDS),* vol. 4, 05/04 2014, doi: 10.11591/ijpeds.v4i3.5883.
[18] R. Latha, S. Babu, and V. Kumar M, "Design and Analysis of Multi-Device Interleaved Boost Converter Driving an Induction Motor," *IOP Conference Series: Earth and Environmental Science,* vol. 850, p. 012036, 11/01 2021, doi: 10.1088/1755-1315/850/1/012036.
[19] L. Zhao, J. Qian, and T. Instruments, "DC-DC Power Conversions and System Design Considerations for Battery Operated System," *Texas Instruments Seminar,* 01/01 2006.
[20] S. Monzer Al, M. Joeri Van, and G. Hamid, "DC/DC Converters for Electric Vehicles," in *Electric Vehicles*, S. Seref Ed. Rijeka: IntechOpen, 2011, p. Ch. 13.
[21] A. S. Abdelrahman, Z. Erdem, Y. Attia, and M. Z. Youssef, "Wide Bandgap Devices in Electric Vehicle Converters: A Performance Survey," *Canadian Journal of Electrical and Computer Engineering,* vol. 41, no. 1, pp. 45-54, 2018, doi: 10.1109/CJECE.2018.2807780.
[22] M. Forouzesh, Y. P. Siwakoti, S. A. Gorji, F. Blaabjerg, and B. Lehman, "Step-Up DC–DC Converters: A Comprehensive Review of Voltage-Boosting Techniques, Topologies, and Applications," *IEEE Transactions on Power Electronics,* vol. 32, no. 12, pp. 9143-9178, 2017, doi: 10.1109/TPEL.2017.2652318.
[23] M. Kabalo, B. Blunier, D. Bouquain, and A. Miraoui, "State-of-the-art of DC-DC converters for fuel cell vehicles," in *2010 IEEE Vehicle Power and Propulsion Conference*, 1-3 Sept. 2010, pp. 1-6, doi: 10.1109/VPPC.2010.5729051.
[24] M. Azri, N. H. A. Khanipah, M. A. M. Nasir, Z. Ibrahim, A. Alias, and N. A. Rahim, "Hardware in the Loop (HIL) simulation of Multi Device Interleaved Boost Converter (MDIBC)," in *2016 IEEE International Conference on Power and Energy (PECon)*, 28-29 Nov. 2016, pp. 155-159, doi: 10.1109/PECON.2016.7951551.
[25] R. B. K. a. B. A. Rao, "INTERLEAVED BOOST CONVERTER," *International Journal of Electrical and Electronic Engineering & Telecommunications,* vol. 1, pp. 305-210, March 2015, doi: 10.18178/ijeetc.
[26] M. S. Hossain Lipu *et al.*, "Review of Electric Vehicle Converter Configurations, Control Schemes and Optimizations: Challenges and Suggestions," *Electronics,* vol. 10, p. 477, 02/17 2021, doi: 10.3390/electronics10040477.
[27] D. Han, J. Noppakunkajorn, and B. Sarlioglu, "Comprehensive Efficiency, Weight, and Volume Comparison of SiC- and Si-Based Bidirectional DC–DC Converters for Hybrid Electric Vehicles," *IEEE Transactions on Vehicular Technology,* vol. 63, no. 7, pp. 3001-3010, 2014, doi: 10.1109/TVT.2014.2323193.
[28] G. Calderon-Lopez and A. J. Forsyth, "High power density DC-DC converter with SiC MOSFETs for electric vehicles," in *7th IET International Conference on Power Electronics, Machines and Drives (PEMD 2014)*, 8-10 April 2014 2014, pp. 1-6, doi: 10.1049/cp.2014.0463.

[29] E. A. Jones, F. F. Wang, and D. Costinett, "Review of Commercial GaN Power Devices and GaN-Based Converter Design Challenges," *IEEE Journal of Emerging and Selected Topics in Power Electronics,* vol. 4, no. 3, pp. 707-719, 2016, doi: 10.1109/JESTPE.2016.2582685.

[30] T. Ayalew, "SiC Semiconductor Devices Technology, Modeling, and Simulation," Dissertation 2.1.1 Crystallography, 2004.

[31] D. Han, S. Li, W. Lee, and B. Sarlioglu, "Adoption of wide bandgap technology in hybrid/electric vehicles-opportunities and challenges," in *2017 IEEE Transportation Electrification Conference and Expo (ITEC)*, 22-24 June 2017, pp. 561-566, doi: 10.1109/ITEC.2017.7993332.

[32] M. Sasagawa, T. Nakamura, H. Inoue, and T. Funaki, "A study on the high frequency operation of DC-DC converter with SiC DMOSFET," in *The 2010 International Power Electronics Conference - ECCE ASIA* -, 21-24 June 2010, pp. 1946-1949, doi: 10.1109/IPEC.2010.5542089.

[33] A. A. ELECTRONICS, "What is Gallium Nitride (GaN) ? GaN in Electronics," 2020, September 6. [Online]. Available: https://www.youtube.com/watch?v=pCVtudewe_4.

[34] T. Hashimoto, M. Shiraishi, N. Akiyama, T. Kawashima, T. Uno, and N. Matsuura, "System in Package (SiP) With Reduced Parasitic Inductance for Future Voltage Regulator," *IEEE Transactions on Power Electronics,* vol. 24, no. 6, pp. 1547-1553, 2009, doi: 10.1109/TPEL.2009.2013225.

[35] J. Millán, P. Godignon, X. Perpiñà, A. Pérez-Tomás, and J. Rebollo, "A Survey of Wide Bandgap Power Semiconductor Devices," *IEEE Transactions on Power Electronics,* vol. 29, no. 5, pp. 2155-2163, 2014, doi: 10.1109/TPEL.2013.2268900.

[36] C. Abboud, M. Chahine, C. Moussa, H. Kanaan, and E. Rachid, *Modern power switches: The Gallium Nitride (GaN) technology*. 2014, pp. 2203-2208.

[37] "Power GaN: the next wave…," *Yole group,* 2022, June 08. [Online]. Available: https://www.yolegroup.com/press-release/power-gan-the-next-wave/.

[38] D. M. Bellur and M. K. Kazimierczuk, "DC-DC converters for electric vehicle applications," in *2007 Electrical Insulation Conference and Electrical Manufacturing Expo*, 22-24 Oct. 2007, pp. 286-293, doi: 10.1109/EEIC.2007.4562633.

[39] "Boost converter," *Wikipedia,* no. Operation, Circuit analysis. [Online]. Available: https://en.wikipedia.org/wiki/Boost_converter.

[40] "Boost Converters," *Learnabout electronics,* 2020. [Online]. Available: https://learnabout-electronics.org/PSU/psu32.php.

[41] A. Ullah, S. Khan, and S. Zhaoyun, "Power Factor Control Using Boost Type Converter," in *2018 IEEE 3rd Advanced Information Technology, Electronic and Automation Control Conference (IAEAC)*, 12-14 Oct. 2018 2018, pp. 54-60, doi: 10.1109/IAEAC.2018.8577767.

[42] "Boost Converter | Step Up Chopper," *Electrical4U,* 2021, May 23. [Online]. Available: https://www.electrical4u.com/boost-converter-step-up-chopper/.

[43] T. Europe, "Toyota and the success of hybrid vehicles," 2020. [Online]. Available: https://www.toyota-europe.com/world-of-toyota/feel/environment/better-air/hybrid-vehicle.

[44] Mitch Olszewski, "EVALUATION OF THE 2010 TOYOTA PRIUS HYBRID SYNERGY DRIVE SYSTEM," *Oak Ridge National Laboratory,* March 2011.

[45] S. Öztürk, "Design of three phase interleaved DC/DC boost converter with all SiC semiconductors for electric vehicle applications," in *2017 10th International Conference on Electrical and Electronics Engineering (ELECO)*, 30 Nov.-2 Dec. 2017 2017, pp. 355-359.

[46] "STTH6010-Y Automotive 1000 V, 60 A Ultrafast Diode," Automotive-grade ultrafast diode PSpice models (.lib & .olb). [Online]. Available: https://www.st.com/en/diodes-and-rectifiers/stth6010-y.html#cad-resources.
[47] Infineon, "IRGPS60B120KD datasheet." [Online]. Available: https://www.infineon.com/dgdl/Infineon-IRGPS60B120KD-DataSheet-v01_00-EN.pdf?fileId=5546d462533600a40153565a56b824a1.
[48] STMicroelectronics, "STTH6010-Y datasheet." [Online]. Available: https://www.st.com/en/diodes-and-rectifiers/stth6010-y.html.
[49] STMicroelectronics, "Calculation of turn-off power losses generated by an ultrafast diode." [Online]. Available: https://www.st.com/resource/en/application_note/dm00380483-calculation-of-turnoff-power-losses-generated-by-a-ultrafast-diode-stmicroelectronics.pdf.
[50] Micrometals, "design-and-applications/design-tools/inductor-designer." [Online]. Available: https://www.micrometals.com/design-and-applications/design-tools/inductor-designer/.
[51] X. Ma, Y. Wang, and P. Wang, "A High Frequency 40kW Step-Up Converter for Fuel Cell Electrical Vehicles Based on SiC MOSFET," in *2019 22nd International Conference on Electrical Machines and Systems (ICEMS)*, 11-14 Aug. 2019, pp. 1-6, doi: 10.1109/ICEMS.2019.8922169.
[52] Wolfspeed, "1200 V Discrete Silicon Carbide MOSFETs," Products/C3M0032120K. [Online]. Available: https://www.wolfspeed.com/1200v-silicon-carbide-mosfets/#product-table.
[53] STMicroelectronics, "1200 V, 40 A High Surge Silicon Carbide Power Schottky Diode," CAD Resources/STPSC40H12C. [Online]. Available: https://www.st.com/en/diodes-and-rectifiers/stpsc40h12c.html#cad-resources.
[54] G. Systems, "GS-065-060-5-T-A , 650V Automotive E-Mode GaN Transistor." [Online]. Available: https://gansystems.com/gan-transistors/gs-065-060-5-t-a/.
[55] M. Moradpour and G. Gatto, "Controller Design of a New Universal Two-Phase SiC-GaN-Based DC-DC Converter for Plug-in Electric Vehicles," in *2018 IEEE 18th International Power Electronics and Motion Control Conference (PEMC)*, 26-30 Aug. 2018, pp. 236-241, doi: 10.1109/EPEPEMC.2018.8521884.
[56] M. Moradpour and G. Gatto, "Efficiency Analysis of Two DC-DC Universal Converters for Electric Vehicles: Single-Phase Paralleled GaN and Two-Phase SiC-GaN-Based," in *2019 21st European Conference on Power Electronics and Applications (EPE '19 ECCE Europe)*, 3-5 Sept. 2019, pp. P.1-P.7, doi: 10.23919/EPE.2019.8915117.
[57] M. Moradpour and G. Gatto, "A New SiC-GaN-Based Two-Phase Interleaved Bidirectional DC-DC Converter for Plug-In Electric Vehicles," in *2018 International Symposium on Power Electronics, Electrical Drives, Automation and Motion (SPEEDAM)*, 20-22 June 2018, pp. 587-592, doi: 10.1109/SPEEDAM.2018.8445373.